PRECISION ENGINEERING CENTER

2005 INTERIM REPORT
September 2005

Sponsors:

3M Corporation
Electro-Optics Center at Pennsylvania State University
Los Alamos National Laboratory
Missile Defense Agency
National Aeronautics and Space Administration
National Science Foundation
Optical Research Associates
Precitech Precision, Inc.
Sandia National Laboratory
Vistakon, Johnson & Johnson Vision Care Inc.

Faculty:

Thomas Dow, Editor
Greg Buckner
Jeffrey Eischen
Paul Ro
Phillip Russell
Ronald Scattergood
David Youden

Graduate Students:

David Brehl
Nathan Buescher
Karalyn Folkert
Timothy Kennedy
Lucas Lamonds
Nadim Wanna
Robert Woodside
Yanbo Yin

Undergraduate Students:

Robert Powell

Staff:

Kenneth Garrard
Karl Falter
Lara Masters
Alexander Sohn

TABLE OF CONTENTS

1 DESIGN OF REFLECTIVE OPTICAL SYSTEMS

Nadim Wanna
Graduate Student
Thomas Dow
Professor
Department of Mechanical and Aerospace Engineering

1.1 INTRODUCTION

Optical systems play a crucial role in a wide variety of products from camera phones to seeker missile guidance systems to free-space optical interconnects on computer chips. The field is divided into major categories: Geometric Optics is the study of light without diffraction or interference whereas Physical Optics expands the scope to include diffraction effects. Whereas some optical systems use reflective, refractive and diffractive elements, the emphasis here will be on reflective systems.

The goal of the first optical design is to gain familiarity with optical design, fabrication and performance evaluation for telescope systems constructed using reflective mirrors. Because changes are most efficiently made during the design process, an understanding of the whole process (design, fabrication, metrology and assembly) must be addressed to are a key to cost effective deployment of system. A telescope system using two mirrors was selected for the first prototype because it is the simplest example of a reflecting telescope. The specification of the system are an entrance pupil diameter of 150mm, effective focal length of 860mm, field of view of 1º, f-number of 5.73, and an image height of 15mm. The second protype will be a similar design but using Three Mirror Antistigmat (TMA) design with the same specifications.

1.2 TWO MIRROR CONFIGURATION

The classic Cassegrain uses a two-mirror layout that consists of a primary and a secondary mirror. The mirrors are coaxial and each mirror is rotationally symmetrical about this axis. Light enters the system, first encountering the primary mirror, which then reflects the light to the secondary mirror. The secondary reflects light through a hole in the center of the primary to the image plane as shown in Figure 1. The primary mirror aperture is specified by the entrance pupil diameter at 150mm, while the f-number of the primary is specified as f/1; thus, setting the radius of curvature of the primary at 300mm.

The Ritchey-Chrétien telescope differs from the two-mirror Cassegrain prescription such that specific optical aberrations are corrected. In this configuration, both aspheres are hyperbolic and correct simultaneously for both spherical aberrations and coma. Like the Cassegrain the Ritchey-Chrétien design is limited by astigmatism at high field angles.

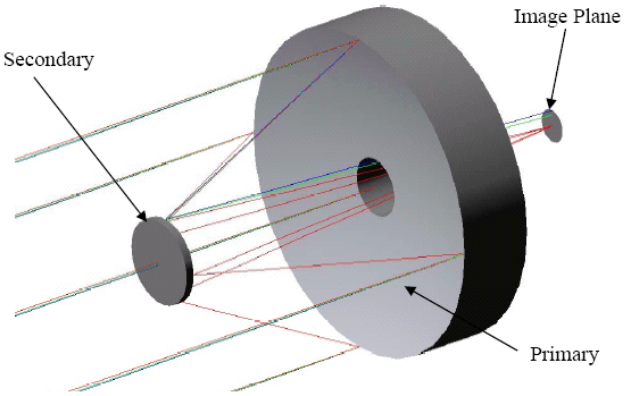

Figure 1. Two mirror optical system

1.2.1 OPTIMIZATION

Global system specifications are used in Code V to initialize the system and solve basic system parameters. The entrance pupil is set to be the same as the primary aperture, 150mm. Because astigmatism is a function of field height in all two-mirror designs, this system is specified at 1º field angle. Paraxial image solve is enabled such that the image surface is set at the system paraxial image focus, or the point where the rays parallel to the system axis converge.

ORA provide a standard optimization routine in Code V that is fully customizable. Third order spherical aberration and third order tangential coma are both targeted to zero. Additionally, the YZ Paraxial marginal exit angle between the secondary and the detector is targeted to 0.0872. This value is determined by the final image height (size of the detector), field angle and the entrance aperture diameter. These parameters also set the f-number of the system, 5.73.

All specifications not explicitly selected are allowed to vary during optimization. The final conic constant of the primary is -1.0048 and the secondary is -2.166. Radius of curvature of the secondary is 89.56mm with an aperture diameter of 39.368mm. Distance between the primary and secondary vertices was adjusted by trial and error to 113.625mm which set the distance from the secondary to the image plane at 208.519mm to accommodate the digital camera to be used as a detector. The effective focal length of the finalized system is 859.872mm.

1.2.2 THEORETICAL PERFORMANCE

System analysis was performed using tools in Code V to predict the performance of the two-mirror system. A Ritchey-Chrétien's fundamental aberration is uncorrectable astigmatism. Astigmatism occurs when a point source is imaged as two separate lines at different axial positions with an elliptical or circular blur between them. For the rotationally symmetric optical system, astigmatism is zero on-axis and increases with the field angle.

Field plots reveal astigmatism and distortion field curves for rotationally symmetric systems by plotting these values over the full field angles in Figure 2. The length of the line segments indicate the magnitude of the astigmatism. The on-axis rays show no astigmatism and the corner rays show the maximum value of approximately each line shows the amplitude and of the astigmatism and the relationship between the shows the sagittal and tangential field curvatures, in which the astigmatism is zero for one zone of the field, on-axis. This point is called the node, and the two focal surfaces separate quite rapidly beyond the node indicating increased astigmatism. Distortion has a node on-axis and increase with field angle, and reaches a value of 0.1%.

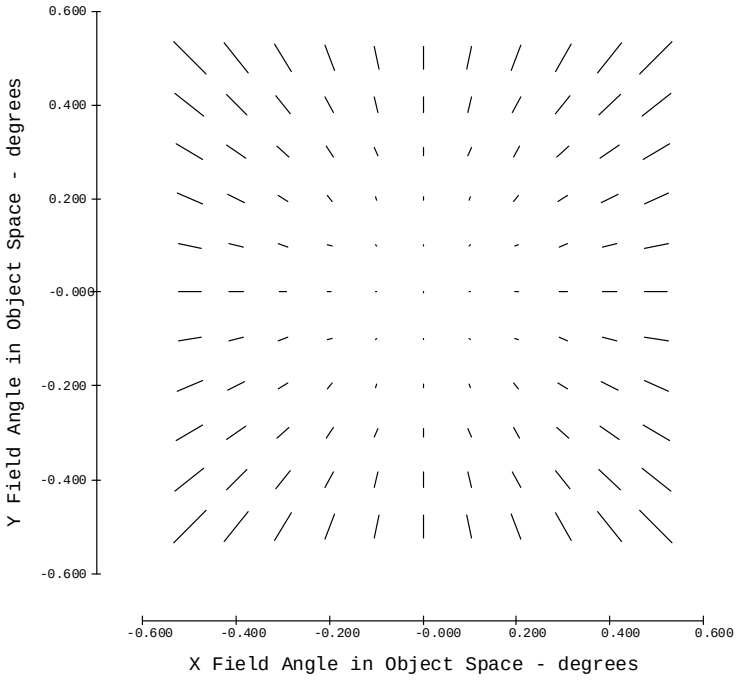

Figure 2. Astigmatism map across the field of view of the telescope (Zernike terms 5 and 6)

When the image plane is at the best focus position, the composite (combined individual field positions) wavefront error is minimized. The 0.35º field position yields the smallest error at 0.1695 λ RMS. The optical axis and full field positions have a value less than 0.7 λ RMS.

1.2.3 OPTOMECHANICAL DESIGN

The design of the structure to support the imaging optics is extremely important in delivering an image quality within the specifications. Figure 3 shows the primary mirror, secondary mirror, and a tube that connects them together. Light entering the telescope from infinity is reflected from the primary mirror's surface onto a secondary mirror 113.625mm from the apex of the primary. The secondary mirror reflects the light through a 26mm hole in the primary mirror onto a detector 72 mm from the back surface of the primary to form the image.

The secondary mirror is held in place through a secondary mirror support structure that locates it relative to the primary mirror. The secondary support structure consists of two parts. First, a tube that is press fit on the primary, providing the required spacing between the mirrors. The interference and axial reference surfaces are shown in Figure 3. Next, the secondary mirror itself which consists of the mirror, an outer ring and three arms that connect them but allow light to enter the telescope. The primary and secondary will be light-press fit on the tube to ensure that the axial reference surfaces meet, thus the distance between the mirror vertices is achieved. The radial interference surfaces insure that the mirrors are coaxial.

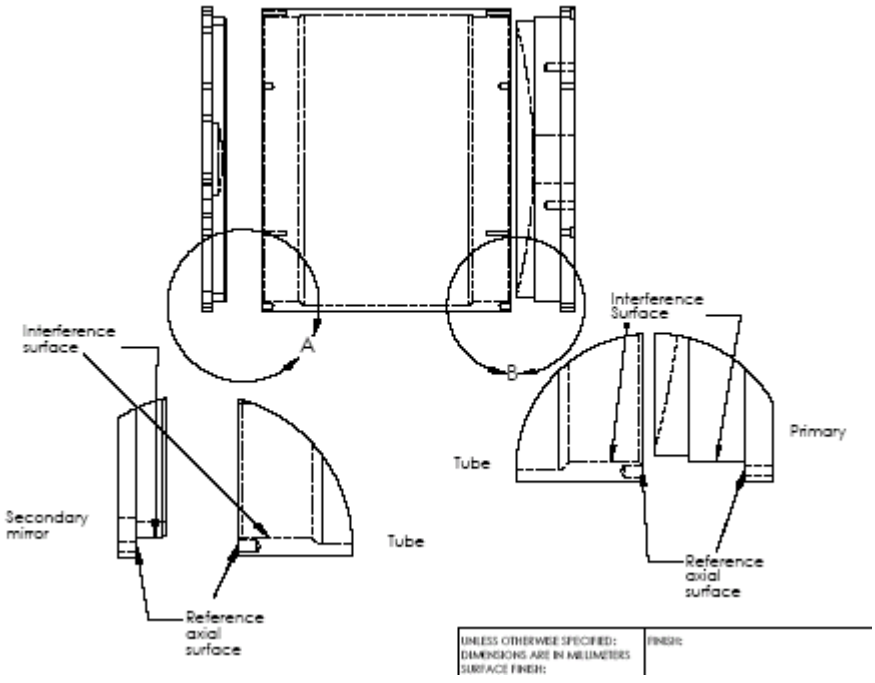

Figure 3. Detail drawing of the telescope

All the components of the telescope are Aluminum 6061. This material combines relatively high strength, low weight, good machinability with diamond tools, excellent coating adhesion and

high resistance to corrosion. Also, by using a single material, no distortion of the components will occur for an environmental temperature change.

1.3 THREE MIRROR

For rotationally symmetric systems, there is no astigmatism on-axis. As the image point moves further from the axis, the amount of astigmatism gradually increases. To avoid astigmatism at a single off-axis field angle, unobstructed three mirror system is considered. The three mirrors would be off-axis conic sections and the system will follow the same specifications as the two mirror design.

Figure 4 shows a schematic of a three mirror telescope using rotationally symmetric conic surfaces. The entrance pupil diameter is 150mm at the primary mirror, but the aperture is decentered in the y-direction. The primary mirror has a radius of curvature of 800mm, and an f-number of 1. The secondary and tertiary mirror shapes and distance between mirrors are allowed to vary during optimization. The same optimization procedure used in the two mirror design is implemented here. The image lies on the optical axis of the system.

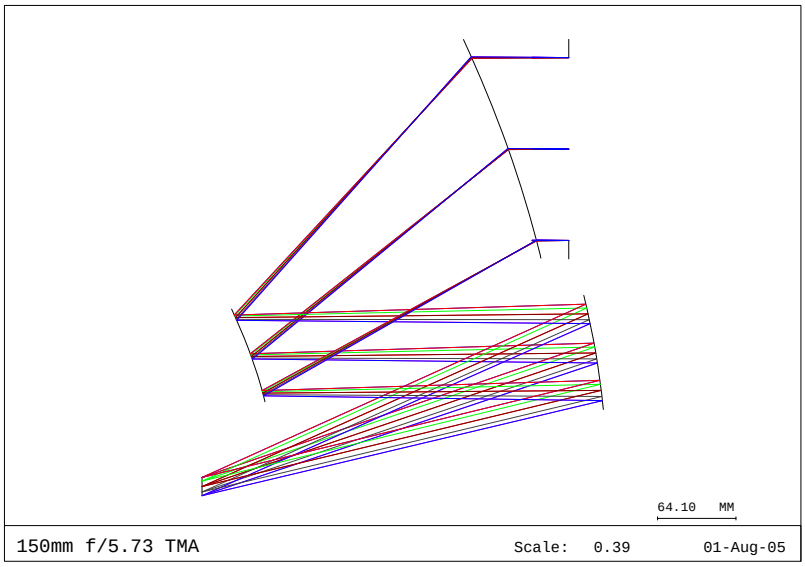

Figure 4. Three mirror anastigmat

Figure 5 shows an astigmatic field map across the 1º field of view of a three mirror anastigmat using off-axis conics. Note there are two nodes (points of zero astigmatism) in the field compared to the single node for the two-mirror design in Figure 2. Distortion and coma also exhibit this node behavior [1]. When the image is at the best focus position (0.35º field position), the resulting wavefront error at 0.0123 λ RMS as compared to 0.1695 for the two-mirror design. This is over an order of magnitude improvement.

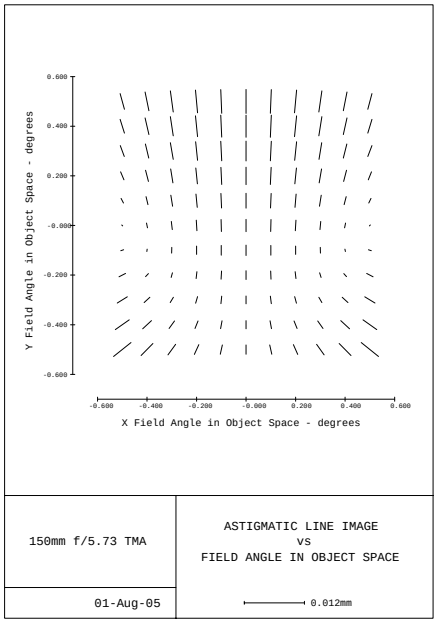

Figure 5. Full field display of astigmatism

To manufacture the optical system shown in Figure 4, the surfaces will be diamond turned around an axis that is through the center of the optic and nominally perpendicular to the surface at the center. This arrangement allows an off-axis shape to be machined on-axis and reduces the size of the machine to create the shape. Typically, a conic surface can be divided into a rotationally symmetric and a non-rotationally symmetric component. The main axes of the DTM (diamond turning machine) are used to create the symmetric component while the FTS (fast tool servo) adds the non-symmetric component. This technical challenge has been addressed at the PEC.

The opto-mechanical design of the three mirror configuration is currently underway. The goal is to package the optical elements such that the appropriate degrees of freedom are constrained but the elements are not over-constrained and thus prone to distortion. An example of a multi-mirror design using off-axis conics is shown in Figure 6. This design uses rectangular aluminum housing with a mirror mounted at each end. The mirrors are individually machined with fiducial features that relate the optical surface to the mounting fixture. The mirrors are each mounted to a sub-frame, which is attached to the housing. Pins and machined flats form the metrology reference frame that relates the optical components to the frame and therefore to each other.

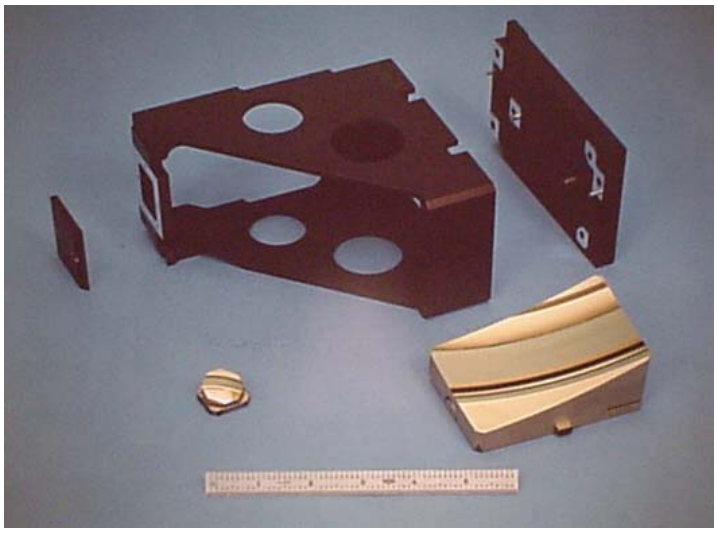

Figure 6. Housing and optics for off-axis optical system (courtesy TI Defense Systems)

1.4 CONCLUSIONS

A two mirror axially symmetric telescope has been designed and optimized. This design suffers from aberrations that increase with field angle and affect the image quality. The opto-mechanical design has been completed to create three main components; a primary mirror, a secondary mirror and a tube that connects them. Sections 4 and 7 of this report address the fabrication and metrology aspects of this design. In addition, a new three-mirror design has been completed. By adding a third mirror in an unobstructed configuration, the aberrations are reduced while holding the same optical specifications. The opto-mechanical design of the TMA is currently in progress.

REFERENCES

1. Rodgers, M. and K. Thompson, “Benefits of Freeform Mirror Surfaces in Optical Design” ASPE Proceedings.

2 METROLOGY ARTIFACT DESIGN

Karalyn F. Folkert
Graduate Student
Thomas A. Dow
Professor
Department of Mechanical and Aerospace Engineering
Kenneth Garrard
Precision Engineering Center Staff

2.1 INTRODUCTION

Coordinate Measuring Machines (CMMs) are widely used to measure the shape of machined parts. Their availability, speed, resolution and flexibility have pushed them into many new applications. Laboratories and manufacturing facilities alike use them to assess the quality of fabricated parts. However, to reap the full benefits of a CMM, there is a need to "qualify" the measuring capabilities and compare it to other available CMMs. Translation of results from one measuring machine to another involves some uncertainty in the size and shape of part features as measured by each machine. Traditionally, a calibration artifact determines the static influences of the machine such as machine geometry. The goal of this project is to design and fabricate a calibration artifact that will test a CMM both statically and dynamically and determine the effects of those influences and produce an uncertainty value for the measurement.

2.2 ARTIFACT DEVELOPMENT

After considering a number of artifact designs, a ring gauge was chosen as the basis for further development. The overall attributes of the ring gauge (outside diameter (OD), inside diameter (ID), and wall thickness) can be used to exercise multiple axes of a CMM. In addition, small features can be added to the ID and OD to assess the capability of the machine to deal with small temporal and spatial variations in surface features. The ring gauge can also be measured in different orientations and positions on the CMM to cover the entire working volume.

2.2.1 SHAPE AND FEATURES

The ring's OD measures 8" (203.2mm) with an ID of 6" (152.4mm) and an overall thickness of 1" (25.4mm). Three counter bores are on one surface with three more counter bores on the

opposite face but rotated 60°. A 45° chamfer is placed on the edge of each counter bore. The chamfers will be used to support 3 steel balls in the horizontal orientation during CMM measurement. Figure 1 illustrates the shape and dimensions of the ring. The material for the final artifact is 17-4 PH stainless steel which was heat treated for maximum dimensional stability. To allow the ring to be diamond machined, it was plated with 150 μm of electroless nickel.

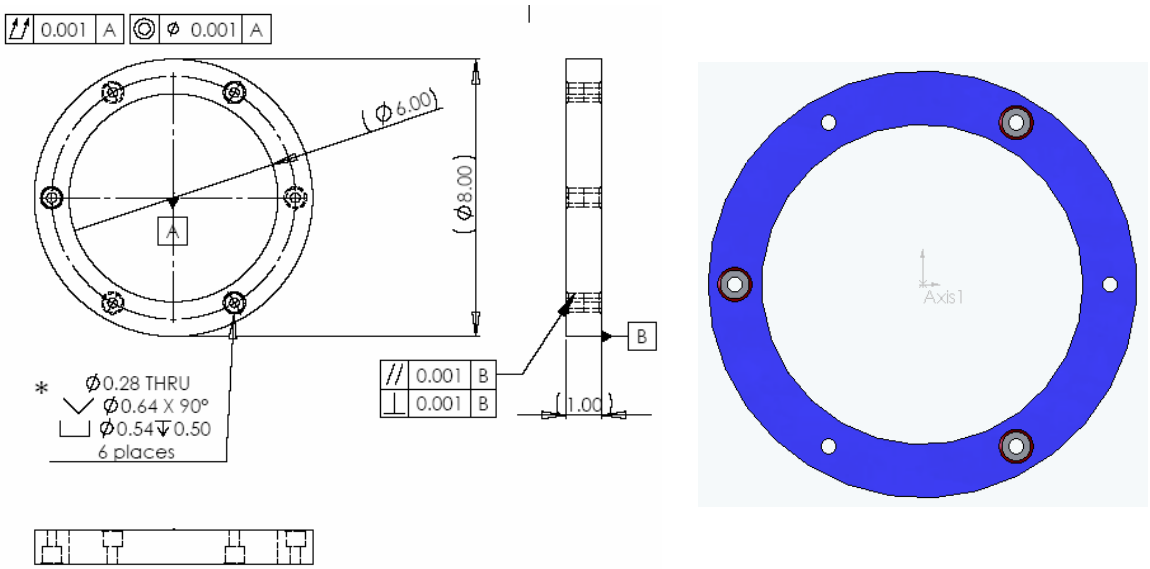

Figure 1. Ring gauge design

Small features are placed on the ID and the OD of the ring to create a range of frequencies for evaluation of the CMM performance in the dynamic environment. The small features chosen are a swept sine wave. A swept sine wave is a sine wave with a continuously varying wavelength; each point on the swept sine wave is a different wavelength.

2.2.2 FABRICATION

The ring was mounted on the DTM on a base disk with three spacers that allow the fast tool servo access to the ID of the ring. The spacers were machined flat before the ring was bolted to them and a minimum torque value was used to avoid distorting the ring. The top surface of the ring was machined flat and the ring was flipped to allow the opposite face to be machined. The final surface finish was 35 nm RMS.

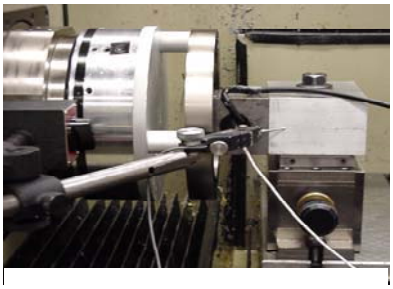

Figure 2. Setup for fabrication of the ID

The fast tool servo (FTS) was attached to the x-axis of the diamond turning machine. It was used to machine a cylindrical surface on the ID and the OD prior to fabrication of the swept sine wave in the center of each surface. To machine the swept sine wave, the FTS operated in closed loop and the DTM at a spindle speed of 20 RPM. This spindle speed was selected to keep the FTS from ringing the lowest natural frequency of the ring. A fiducial was added to the OD surface to act as a once-per-rev reference for the wave. Figure 2 illustrates the setup for fabrication of the ID and the OD of the ring and Figure 3 shows the features machined onto the ring.

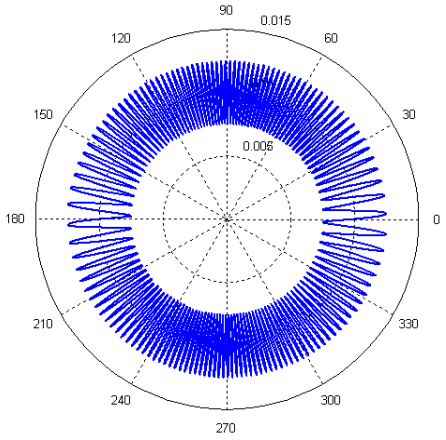

Figure 3. Swept sine wave on the OD/ID of the ring

2.2.3 MEASUREMENT RESULTS

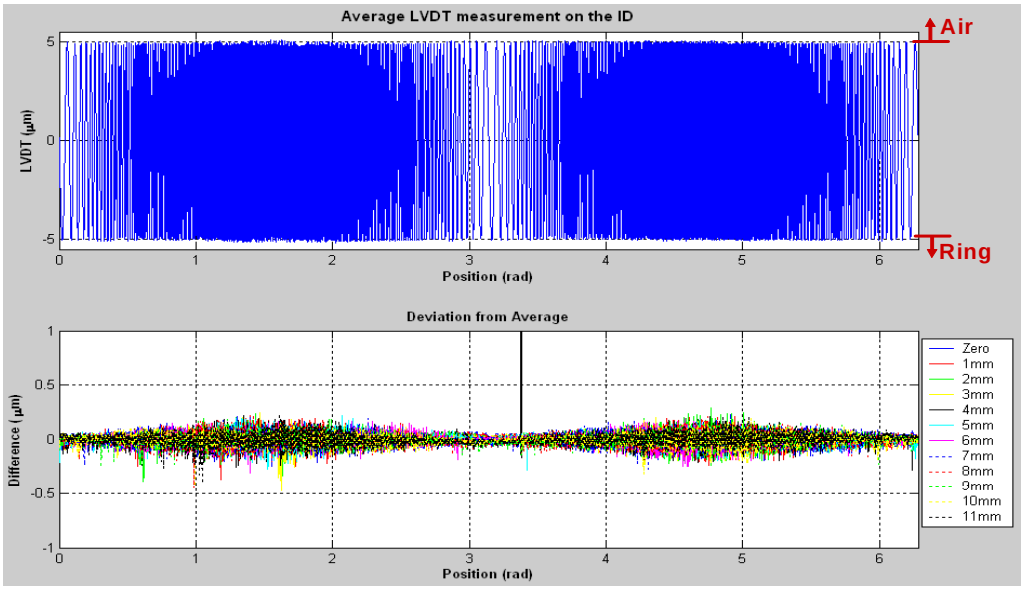

Figure 4. Average of measurements along with wave deviation on the ID of Ring 2

The swept sine waves on each ring were measured with an air-bearing LVDT following fabrication. Twelve measurements were taken at 1 mm increments along the width of the wave. The individual measurements were combined into a single measurement. Figure 4 displays the average measurement of the ID in the top subplot while the bottom subplot shows the deviation of each measurement from the average data set. The roundness of the cylindrical region on each ring was also measured and ranged from 0.12-0.35µm.

Swept Sine Wave Excitation

The minimum and maximum spatial wavelengths were used to generate a range of frequencies that depend on the speed of measurement. Because the wavelengths can be considered as individual frequencies, an FFT can be performed on the data set. With sampled data, the units on the frequency spectrum plot are in terms of Hertz. However, with the generated spatial data, it is more useful to plot the results in terms of wave numbers[1]. The wave number is the reciprocal of the spatial wavelength. Figure 5 shows the FFT of the first quadrant of the ideal wave for the ID. The magnitude is largest near the shortest wavelength at wave number 223/λ which translates to a wavelength of 0.537µm. The phase values accumulate for half of the wavelengths and then return to zero.

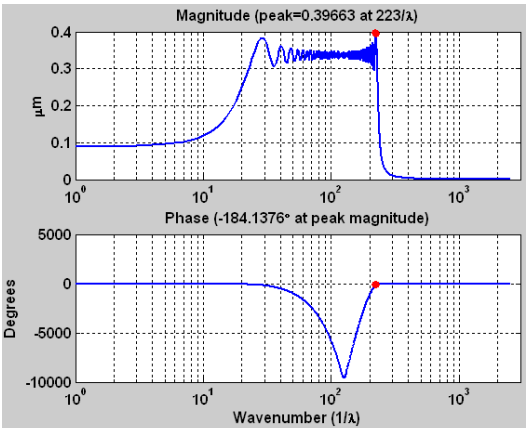

Figure 5. FFT of the first quadrant of the swept sine wave on the ID

The FFT of the swept sine wave is more difficult to interpret than a single frequency sine wave because to the constantly varying nature of the wavelength. Rather than strictly interpreting the FFT and directly comparing it to an FFT of an actual measurement, the data analysis can be simplified. A CMM has dynamic characteristics that will influence the overall measurement of the artifact. Since the swept sine wave on the surface of the ring is known and the CMM

[1] The number of waves per unit distance (quarter of the circumference of the ring).

measurement will generate another data set, the CMM's dynamics, or transfer function, may be found using a form of deconvolution. Convolution in the time domain is the multiplication of the swept sine wave and the impulse response of the dynamic system to construct an output that shows the influence of these dynamics. Since the dynamics of the CMM are not known, the inverse of convolution, or deconvolution, is used; the CMM measurement is divided by the accepted swept sine wave. To expedite calculations, deconvolution may be executed in the frequency domain. The magnitude and phase components in the frequency domain are separated to create a Bode plot of the CMM's dynamics. The left image in Figure 6 is the dynamics of a theoretical 2nd order system and came out of a single measurement using the swept sine wave over a quadrant of the ring gage. The box denotes the range of frequencies from that single measurement and how it can identify the dynamics of the CMM/probe system.

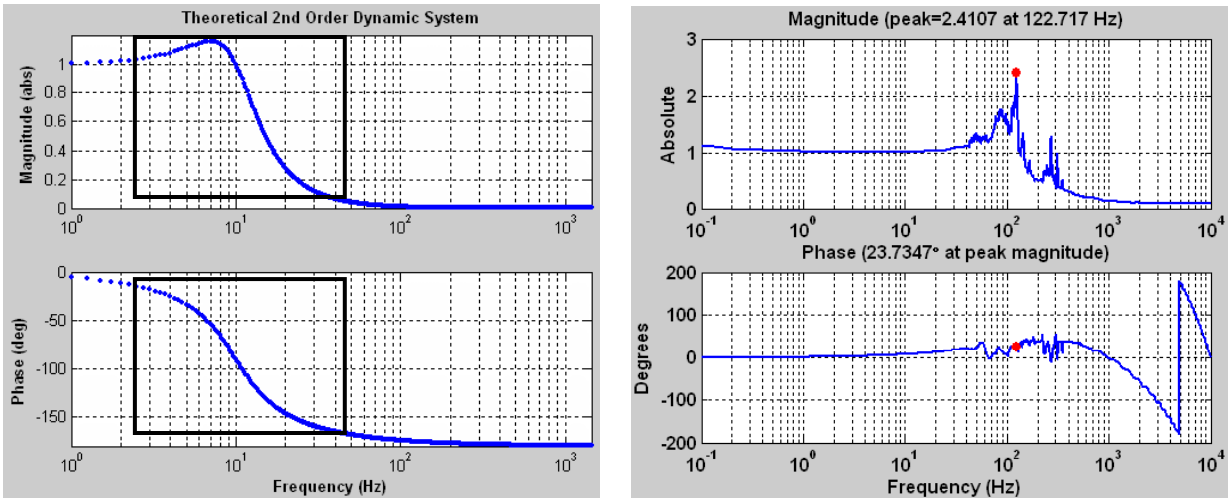

Figure 6. Theoretical second-order dynamic system (left) and measurement of air-bearing LVDT using the swept sine wave features at 1 rpm (right)

The right hand image in Figure 6 is the experimental transfer function of the air-bearing LVDT as measured using the ring gage in the DTM spindle and a spindle speed of 1 rpm. This shows typical spring-mass system response with a peak in the 100 Hz range.

2.3 CONCLUSIONS AND FUTURE WORK

A calibration artifact has been developed. It is a stainless steel ring gauge with a 6" ID, 8" OD and a 1" square cross section that is plated with electroless nickel. The shape of the ring gauge is appropriate for static calibrations. A swept sine wave feature has been machined on the OD and ID with an amplitude of ±5 μm and a spatial wavelength range from 0.45 to 6.5 mm.

The ring gauge artifact was fabricated by diamond turning. All surfaces were diamond machined and a swept sine wave was fabricated on the OD and ID using a fast tool servo. Because of the dynamics of the fast tool servo, deconvolution techniques were needed to improve the fidelity of the sine wave features. The different surfaces of the machined ring were round to 0.2 μm with a surface finish of 37 nm RMS.

The ring gauge artifact was used to find the dynamics of an air-bearing LVDT to demonstrate the procedure for determining the dynamics of a CMM. The 80 Hz natural frequency of the LVDT was successfully derived from gage measurement data; however, specific features of the dynamic response are in question.

3 LIVE-AXIS TURNING

Nathan Buescher
Graduate Student
Thomas Dow
Professor
Department of Mechanical and Aerospace Engineering
Alexander Sohn
Precision Engineering Center Staff

3.1 INTRODUCTION

Diamond turning (DT) has revolutionized optical fabrication because of its ability to accurately and rapidly create spherical and aspherical optical surfaces as well as the opto-mechanical features needed for alignment. An emerging trend in optical design is the use of optical surfaces that are non-rotationally symmetric (NRS). When such surfaces are included in an optical system, the complexity, bulk and weight of the system can be reduced while the performance is improved. However, the production time for these parts is often excessively long due to their complex shape and the slow response speed of the axes of the diamond turning machine. One way to speed up the process is to add a Fast Tool Servo (FTS) or auxiliary axis on the machine to respond more quickly to the changing shape of the surface but such devices typically have stroke limited to less than 1 mm. Fortunately, the shape of these NRS surfaces can be divided into a best-fit sphere or asphere and a NRS component thereby reducing the stroke needed for the FTS. The goal of this project was to develop a new FTS design with increased stroke and resolution while retaining the surface finish and speed of current diamond turning processes.

The Live-Axis Turning (LAT) system takes advantage of recent advances in air-bearing slide design, linear motors, high-resolution encoders and control algorithms to increase the velocity and range of tool motion and demonstrate a commercially viable device that will extend the capability to fabricate high-quality NRS optical surfaces. The goal was to create a tool axis capable of 4 mm displacement at 20 Hz.

3.2 ACTUATOR DESIGN

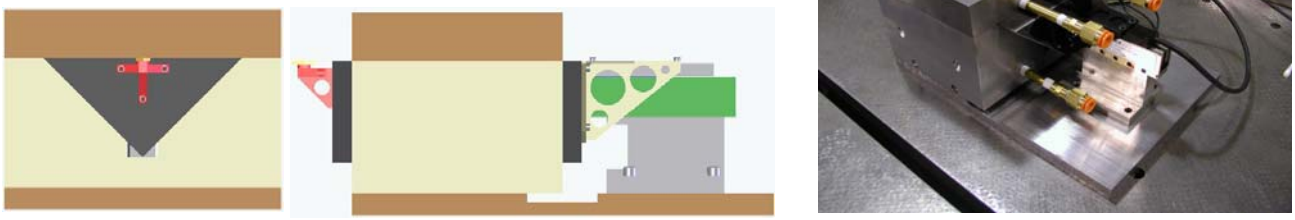

Figure 1. Front and side view drawings of the LAT and a photograph of the finished system

The LAT axis is a light-weight, air bearing, linear motor driven slide that can operate with a stroke of 4 mm at 20 Hz. The piston is triangular in shape and fabricated using a lightweight aluminum-honeycomb construction. It is supported on each side by a stiff air bearings and driven by a linear motor. A holder for a diamond tool is attached to the front of the slide. A drawing and photograph of the LAT system is shown in Figure 1.

Piston Design The main challenge was to create a stiff, lightweight tool holder to support the tool in 5 degrees of freedom while allowing it to move along a single linear axis. The solution was a triangular shaped piston riding in a linear air-bearing. Different piston cross-sections and lengths were studied to find a design that would be both light and stiff with high natural frequencies in the critical directions. The piston was fabricated using sheets of aluminum honeycomb with face and end sheets glued together, anodized and lapped flat. The properties of the honeycomb sheets were calculated and measured, and a model for the piston properties based on modulus and density was constructed. To select an optimum cross-section shape, finite element models were created for different cross-section shapes including a box, a V, and a triangle. The properties of interest were the bending stiffness, mass, first natural frequency, center of gravity, location of the linear motor and location of the position sensing encoder. Piston length is another important design issue because the air-bearing performance improves with increased length but the structural stiffness decreases. After analyzing the changes in natural frequency and the rate of change of air-bearing stiffness with bearing length, a 180 mm slide was selected. Table 1 shows the results of the predicted and measured structural properties of the triangular piston. The predicted mode shape of the first natural frequency was a twisting motion around the central axis of the triangle and the second was a bending mode perpendicular to the central axis.

Table 1: Structural properties of LAT piston and assembly

	Weight, gm	ω_1, (Hz)	ω_2, (Hz)	ω_1/ω_2	ω_{vert}, (Hz)	ω_{ang}, (Hz)
Predicted	445	3950	5110	0.77		
Actual	517	3540	4660	0.76	3400	1900

Motor Selection A brushless linear motor was chosen for its smooth motion characteristics, light weight, high accuracy, repeatability, high acceleration capabilities and stiffness. The force needed to drive the piston (M=0.665 Kg) at target motion (2 mm amplitude at 20 Hz) is 21 N. The Airex Linear Motor P12-1 chosen produces 27 N cont. (84 N peak). The motor accounts for 100 g of the piston's moving mass and can produce peak acceleration up to 13 g's.

Linear Encoder The Renishaw RGH24B steel-tape, linear encoder (20 μm period) provides position feedback to the controller and motor commutation information to the amplifier. The read-head is attached to the structure of the bearing. The tool is in line with the linear encoder so there is no Abbe offset in the position measurement. The 1 V P-P sinusoidal output is interpolated by the UMAC into 4096 counts per period, giving it a theoretical resolution of 5 nm. Unfortunately, a noise level of 2.5 mV on the sine wave signal reduced this resolution to approximately 50 nm.

Air Bearing The triangular piston is supported by a 90º v-block base assembly and a flat top as shown in Figure 1. The base assembly has an air bearing designed by Precitech that incorporates innovations in both the design and fabrication procedure. The bearings in the base assembly were optimized for stiffness and damping in frequency range of the first dominant vibration mode. Static stiffness measurements were made by loading the piston in the vertical direction (300 N/μm) and at one edge (0.2 Nm/μ rad). Air flow with 80 psi applied to the bearing was 90 liter/min with an initial clearance of 45 μm.

3.3 DYNAMIC TESTING

One major concern in attaching the LAT system on top of, and aligned with, the Z-axis of the Nanoform 600 DTM was the effect it would have on the motion of the Z-axis. Initial estimates showed that the impact on the Z-axis would not be significant due to the high stiffness of the Z-axis and the small moving mass of the LAT axis compared to the Z-axis. The stiffness of the Nanoform 600 slide is 60 N/μm and the dynamic displacement with the LAT (piston moving at 2 mm amplitude and 20 Hz) is estimated to be about 350 nm. If this deflection only occurred at the excitation frequency (as it would with a linear system), the result would be an small reduction in the amplitude of the servo motion (~.02%) and that reduction could be compensated with increased gain. However, the low frequency servo motion excites the Z-slide at its natural

frequency (120 Hz) as shown in Figure 2. The relative motion of the Z-slide at its 120 Hz natural frequency (± 200 nm) is larger than its motion at the excitation frequency of 20 Hz (±150 nm). Such high frequency disturbances will have a deleterious effect on the surface finish and some remedy must be developed to reduce this effect. Several ideas including counter-balance masses and tuned dampers will be examined in a later phase of the project.

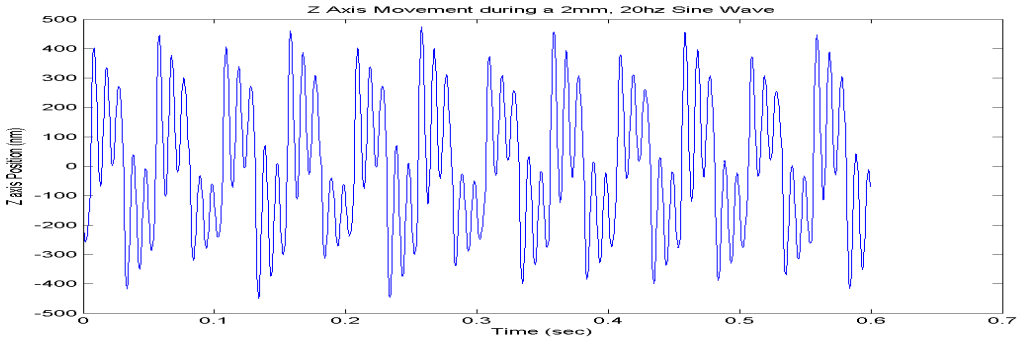

Figure 2. Motion of the Z-axis of the DTM with the LAT performing a 2 mm, 20 Hz sine wave

3.4 CONTROL SYSTEM DEVELOPMENT

The LAT system was integrated into the Nanoform 600 diamond turning machine for the machining experiments. The machine controller, a Delta Tau Turbo UMAC, allowed this new axis to be added to the system without compromising performance or flexibility. The controller for the LAT axis must know the positions of the other axes, including the spindle to produce the commands for a freeform optical surface. The other reason for using the Delta-Tau UMAC is that a high-resolution encoder interpolator accessory board was available on the controller. The 2.3 kHz UMAC cycle update was deemed acceptable for controlling a system with an expected closed-loop natural frequency of less than 1/10th of the controller frequency. Finally, the UMAC includes all the trajectory generation code necessary for specifying a toolpath for the LAT axis.

Open loop testing was first performed to characterize the system and to create a model to study potential control algorithms. Since the LAT system has a mass driven by a linear motor with little or no friction from the air bearing, a sinusoidal current input (force) signal is expected to produce an decreasing output amplitude (40 dB/decade) with a constant 180° phase shift. The measurement confirmed this result and indicated no mechanical resonances at frequencies below 1000 Hz.

Closing the control loop involved tuning the controller to produce the best possible response without going unstable. Initial loop tuning was performed using step function testing to minimize rise time while maintaining a damping coefficient of approximately 0.3. Proportional, derivative, and integral gains were all optimized to achieve this goal. Additionally, acceleration and velocity feedforward gains were optimized to achieve the best possible following error in a parabolic move command. The final closed loop natural frequency is about 100 Hz and the bandwidth of the actuator (-3 dB amplitude ratio) is about 200 Hz which is significantly better than the target of 70 Hz. The response is flat to above 50 Hz and the phase lag is less than 5º.

3.5 MACHINING EXPERIMENTS

Two sets of cutting tests were performed: machining a flat surface and machining a tilted flat.

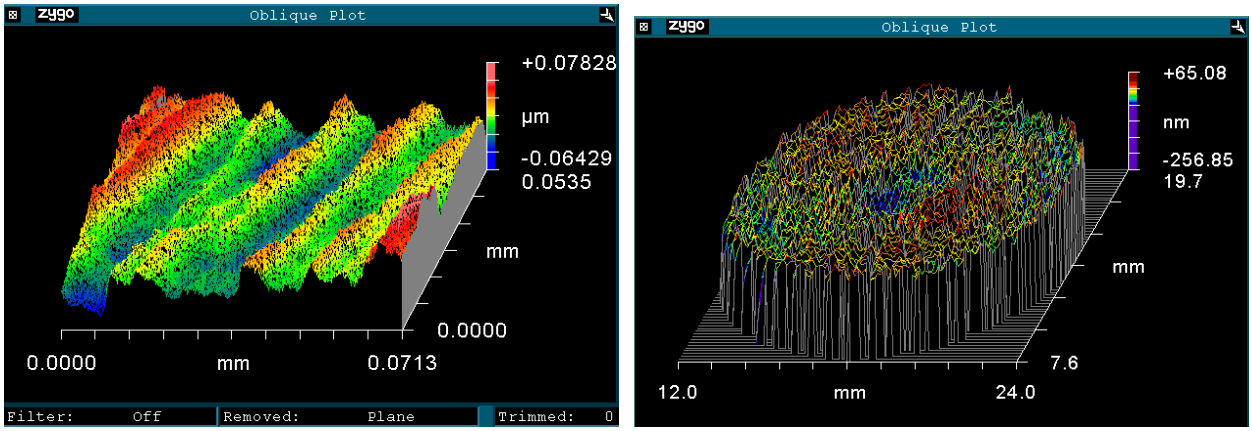

Figure 3. SWLI image of surface finish (Ra=16 nm) and overall figure error (λ/2) of 12 mm diameter copper flat.

Flat Surface The flat was machined to test the ability of the LAT axis to hold position while machining. The flat was cut at 500 rpm with a 1 mm/min feedrate (2 µm/rev) and 5 µm finish pass depth of cut. The Scanning White Light Interferometer (SWLI) measurements in Figure 3 shows 50 X 70 µm patch represents approximately 35 tool passes with a surface finish of 16 nm (Ra).

Figure 3 also shows a Zygo laser interferometer image of the entire part. The figure shows the part's deviation from a perfect flat. The PV form error over the entire part is 321 nm (Ra 27 nm), which is less than ½ wave. This value is very close to the observed PV motion of the slide during position holding and thus is the limiting factor in achieving better finishes.

Tilted Flat A second experiment involved the creation of a tilted flat. The LAT slide moves the tool in a sine wave with one cycle per rotation of the part. As the tool moves from the OD to ID, the amplitude will decrease linearly to create a flat surface that is tilted with respect to the spindle face. This experiment exercises the full range of motion of the tool servo but creates a surface that is easy to measure and interpret.

The results from an aluminum workpiece are shown in Figure 4. The surface finish is shown on the left and the figure error through the center of the part is shown at the right. The 25 mm diameter surface was machined at a fixed speed of 300 rpm, 2.5 mm/min feedrate (5 µm/rev), 5 µm final pass depth of cut and ± 1 mm tilt. The surface finish shown in Figure 4 is slightly higher than the flat at 20 nm Ra. The figure error through the center of the tilted flat (which should be parallel to the base and thus zero) is tilted as shown at the right in Figure 4 and the maximum error is about 70 µm. Clearly this could be smaller (± 5 µm) if the tilt is removed but the error shown has been related to a non-linearity in the actuator.

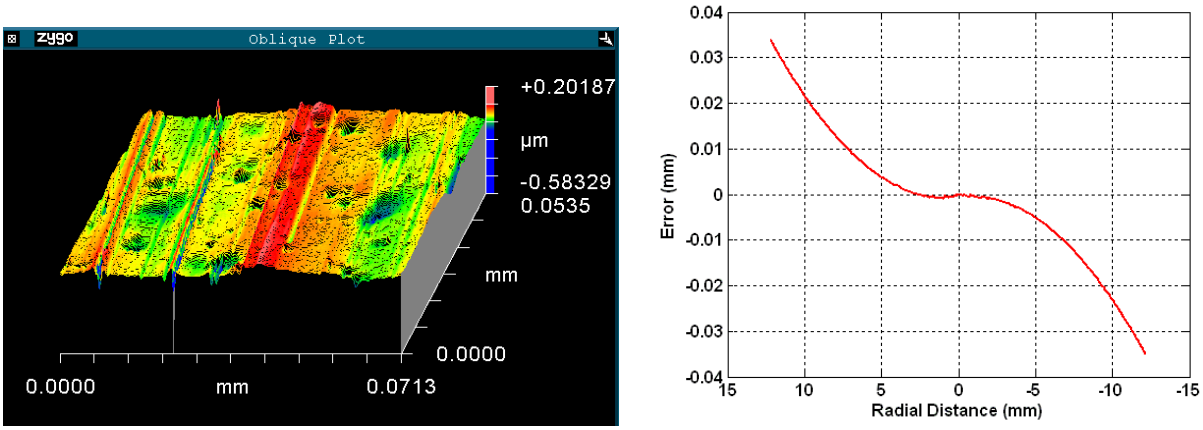

Figure 4. Surface of the aluminum tilted flat measured by the SWLI (left) and error through the center of the flat measured on a Talysurf (right)

Figure 5 shows a model of the tilted flat (left) and the error attributable to a phase angle (right) that is a function of the speed of the LAT axis. Such an error has been observed in other long range actuators such as the piezoelectrically-driven Variform. The image at left is the tilted flat showing the ±1 mm tilt in the x direction. The right image is the error between the perfect tilted flat and a tilted flat with a linear change in phase with velocity - the maximum being only 2º at the OD. Note that the error is largest in a plane that is at right angles to the tilted surface. This is because the error is proportional to velocity and that is 90º out of phase with the displacement. While this error is large, once it is identified, deconvolution can be used to modify the input signal and reduce the value significantly.

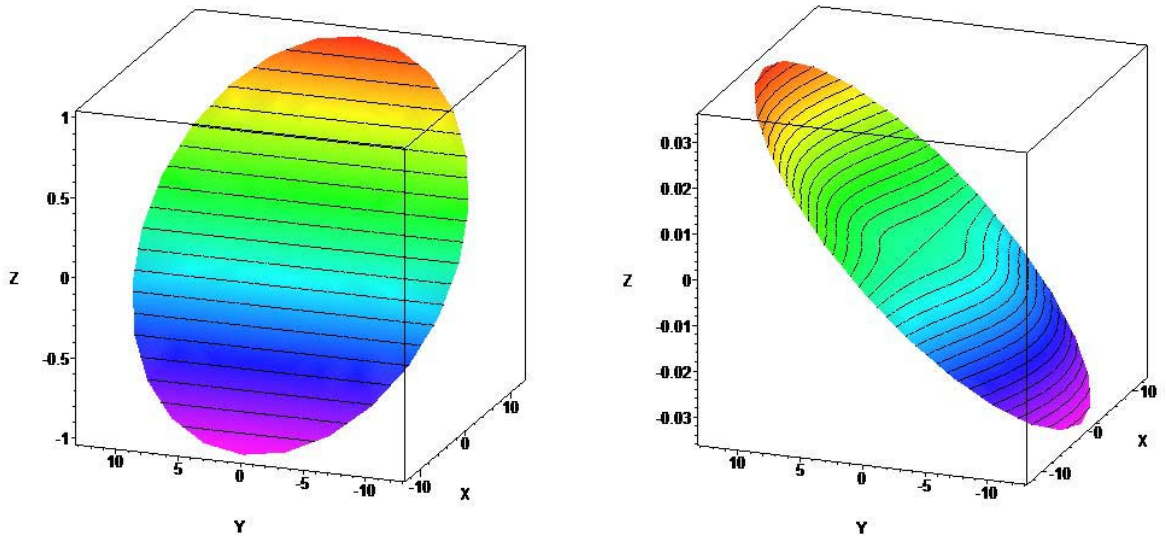

Figure 5. Error due to a linear change in phase with amplitude with a maximum of 2º at OD

3.6 CONCLUSIONS AND FUTURE WORK

The surface finish and figure error for the prototype LAT actuator are not acceptable for finish machining of optical surfaces. However, a number of concerns have been identified and solutions to those are in progress. These issues and techniques to address them are:

- Encoder noise and resolution – The long-range, high speed LAT axis is a challenge for a linear encoder because the data rate cannot exceed the clock of the encoder electronics The 20 μm period of the Renishaw steel tape is relatively long and, coupled with noise on the sine waves, reduces the resolution to greater than 50 nm. The solution for the prototype is to add a laser interferometer with high-resolution, parallel-data position feedback and for next generation LAT axes is to use a shorter period glass scale.
- Vibration of machine axis – The mass of the LAT axis running at 20 Hz excites the natural frequency of the Z slide of the DTM. One solution is to reduce the mass of the slide (next generation design) and another is to add a second mass to counter balance the slide mass.
- Noise in PWM amplifier – The Pulsed Width Modulated power supply for the LAT motor has significant noise and this can excite the slide and degrade the surface finish. A linear amplifier will be substituted.
- Non-linear slide motion – A non-linearity has been identified in the LAT slide; that is, the phase angle (following error) is a function of the speed of the slide. This creates a relatively large error for a small phase angle. However, with an understanding of the source of the error, it can be eliminated with a modified input signal.

4 SIMULATION OF MANUFACTURING ERRORS FOR FREE-FORM OPTICS

Alexander Sohn
Kenneth P. Garrard
Precision Engineering Center Staff
Thomas A. Dow
Professor
Department of Mechanical and Aerospace Engineering
T. Bruegge
Optical Research Associates

4.1 INTRODUCTION

Freeform optical surfaces can be used to control astigmatism at multiple locations in an image. As a result a freeform surface may replace multiple spherical and aspheric reflective components in a complex optical system. Unfortunately, designers have been reluctant to use freeform or even aspheric surfaces in part because they are unable to ascertain the quality of the parts that would be made using diamond turning. A project is under way with Optical Research Associates (ORA), the producers of CODE V, to remedy this obstacle by providing feedback to the designer on the manufacturability of an optical surface as part of the design process.

Machining errors in diamond turning of free-form optics (specifically those fabricated using a servo axis) fall into two categories: dynamic errors and geometric errors. Dynamic errors can be estimated by characterizing the dynamic system response of the machining system, inserting those dynamics into a toolpath and thus generating an error profile. Geometric errors are those that are dependent on machining parameters such as tool geometry, axis straightness, scale errors and angular errors (roll, pitch and yaw). Both types of errors can have a significant influence on the final part, though their significance is heavily dependent on the particular part being fabricated. Ultimately, it is the errors' influence on the optical performance of a system that is of interest. This can be estimated by calculating the surface errors and inserting a simulated, flawed surface into the optical system and observing the change in the optical performance.

4.2 DYNAMIC ERRORS

Dynamic error estimation for off-axis conic surfaces and their influence on optical performance has been calculated and is now available in CODE V® optical design software [1]. These errors

are dependent on the measured dynamics of each servo axis. A more responsive axis (higher bandwidth) will exhibit lower dynamic errors, but typically has less range than a more sluggish axis. Dynamic errors are only applied to the non-rotationally symmetric (NRS) portion of the surface shape is determined using decomposition. Each surface point will be shifted in amplitude and phase and combined with the previously calculated errors to reveal a simulation of what the surface would look like when produced with the method chosen by the designer. Extension of this capability is in progress.

4.3 GEOMETRIC ERRORS

Geometric errors can be divided into two categories: tool errors and machine errors. Machine errors typically are those associated with straightness, angular, and scale errors in the axes of a machine and must be calculated from measurements of these errors on the machine. Their implementation is very machine-specific and can vary significantly with parameters such choice of tool offset and part mounting method. Axis straightness figures for modern diamond turning machines tend to be less than 500 nm over the entire axis travel. Once again, the influence of these figures on the final part is heavily dependent on part geometry. Smaller parts with less sag tend to be affected much less than larger parts. Scale errors can also be significant, though they also tend to have a lesser influence on the figure error of smaller parts. Sources of these errors can be polarization mixing in heterodyne interferometers or phase alignment in linear encoders.

4.3.1 TOOL ERRORS

The main body of errors addressed in this effort are associated with the cutting tools. Tooling errors can be classified into three components: centering, radius error, and edge waviness. While these components are usually presented separately, they are all actually artifacts of the edge profile in space. The edge profile, including any imperfections in the tool or its location in space are described in the Tool Error File (TEF). The TEF is a series of points in a cylindrical coordinate system with its origin at a programmed tool position. Three columns of data, as shown in Table 1, are generated from a given set of inputs that are either supplied by the user or generated from a database of typical errors. The tool edge is described by the local tool radius R, vertical displacement of the edge y, and the tool angle γ, which is also the contact angle of the tool on the surface to be machined. The TEF can be plotted to show a theoretical tool edge in space as shown in Figure 1. The inputs for generating the tool error file are:

- **Base radius**

  R defines the idealized tool shape used in programming the tool path on the machine.

- **X-centering error**

  The tool radius changes by $R_x = \frac{\partial x}{\sin\gamma}$ as a function of the centering error δx and the tool angle γ.

Table 1 Sample Tool Error File (TEF).

γ (rad)	R (mm)	y (mm)
-0.523598776	-0.136574596	0.136974596
-0.436332313	-0.115803313	0.096692213
-0.34906585	-0.093604122	0.063307379
-0.261799388	-0.070544449	0.037074174
-0.174532925	-0.04717713	0.018192247
-0.087266463	-0.02373909	0.006805302
8.32667E-17	-0.0002	0.003
0.087266463	0.02368909	0.006805302
0.174532925	0.04754713	0.018192247
0.261799388	0.070794449	0.037074174
0.34906585	0.093354122	0.063307379
0.436332313	0.115253313	0.096692213
0.523598776	0.136474596	0.136974596

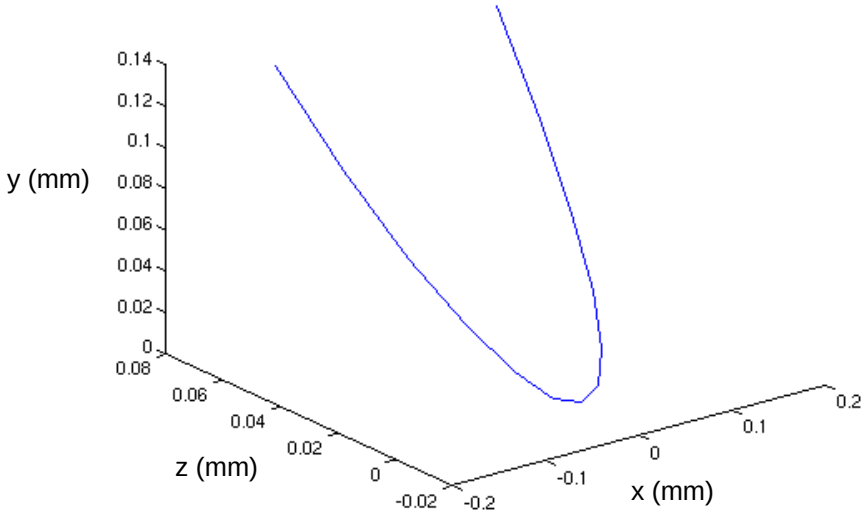

Figure 1. Plot of tool edge error from a sample TEF. Most of the error shown is the result of radius error and rake angle.

- **Y-centering error**

  The y-centering error δy is simply added to all y-values in the TEF
- **Radius error**

  The radius error δR is a constant that is added to all values of R in the TEF.
- **Waviness profile**

  The waviness profile is a series of radius errors $w(\gamma)$ that is added to the TEF as a function of the tool angle γ. Since waviness profiles may not be available to the optical designer, sample waviness profiles are available that can be scaled as a function of the specified waviness specification w.
- **Rake angle**

  The rake angle changes the tool radius as a function of γ:

  $$R(\gamma) = R - R(1-\cos\alpha)\cos\gamma$$

  and the vertical position of the tool edge as a function of γ:

  $$y(\gamma) = R\sin\alpha\cos\gamma$$

Once the TEF has been compiled, its influence on the part profile to be machined can be determined. This process requires turning the part profile into a series of data points in cylindrical coordinates with its axis coincident with the spindle axis. Each of these points has an associated surface slope that will determine which tool angle, and hence radius error, will be associated with the point on the part's surface. The radius error will then cause an offset of that point in both the normal direction and the direction of rotation (θ) of the part surface. This surface with a modified point profile must then be interpolated back to the original point grid to be fed back into CODE V.

4.3.2 TILTED FLAT

A tilted flat is one of the simplest NRS surfaces that can be diamond turned. It is useful to demonstrate some of the types of errors and their impact on the final surface. It can also be used to demonstrate the compatibility of this generalized error estimation scheme with more direct, analytical evaluations that are specific to the surface of interest. For example, looking only at tool radius compensation for a tilted flat, the analytical version of the tool error in the z-direction is:

$$\partial z = \left| \frac{r}{\cos\gamma} - r \right| \tag{1}$$

where, γ is the tool contact angle and r is the tool radius. The tool angle is given by

$$\gamma = \tan^{-1}\left(\frac{A}{R}\cos 2\theta\right) \tag{2}$$

where A is the tilt amplitude, R is the radius of the part, and θ is the angular position of the part. Note that this radius error is independent of the radial (x-axis) position of the tool as shown if Figure 2.

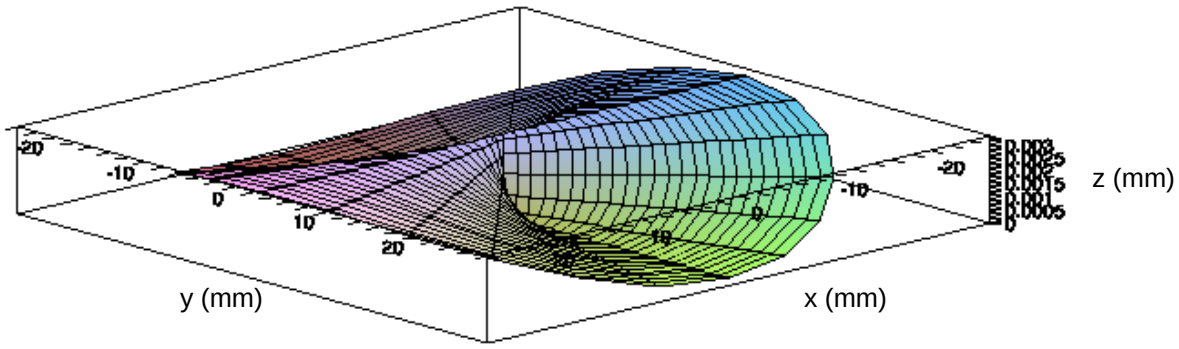

Figure 2. Simulation of radius compensation error on a tilted flat with 4 mm of tilt over a 50 mm diameter. Note lack of dependence on radial position.

When only tool radius error is applied to the TEF and the error is evaluated for a tilted flat with the same amplitude, the same result is obtained. While this does not definitively prove congruence between the two methods for obtaining tool errors, it clearly demonstrates compatibility.

4.4 CONCLUSION

A method for evaluating tool errors in diamond turning free-form optics that is generally applicable to a wide range of surface geometries has been described. This method is intended to aid designers in evaluating the manufacturability of freeform optics through feedback to Code V optical design software. The example of a tilted flat has shown that the errors evaluated from a closed form agree with those obtained through application of the tool error file to an arbitrary surface.

Future work will expand this method to include other geometric errors in the machine such as axis straightness, squareness, roll, pitch, and yaw. Many of these errors as well as tool waviness can be made available from manufacturers' specs to facilitate error estimation and make the process more accurate.

REFERENCE

1. Garrard, K.P., T. Bruegge, J. Hoffman, T. Dow and A. Sohn. Design tools for freeform optics. SPIE 5874 (2005).

5 FABRICATION OF OPTICAL SURFACES AND FIDUCIALS

Lucas Lamonds
Graduate Student
Thomas Dow
Professor
Department of Mechanical and Aerospace Engineering

5.1 INTRODUCTION

This research is oriented toward fabrication of aluminum optical surfaces with a diamond turning machine. Presently, rotationally symmetric conic mirrors are commonly created with a diamond turning machine. The current status of this research is focused on replicating this task by creating the telescope outlined in Section 1. This exercise is intended to prepare for the task of fabricating freeform optic surfaces with a diamond turning machine and a fast tool servo.

5.2 FABRICATION TOLERANCE

The mechanical system of the telescope is designed such that its imaging performance is solely dependant on the magnitude of the optical and fiducial surface fabrication errors. The shape error created by the DTM on flat and spherical components is on the order of λ/4 (150 nm) and tolerance on length or diameter dimension is ±1 μm. CODE V ® provides a tool for calculating manufacturing tolerances from a specified degradation in image quality, a method called 'inverse sensitivity'. Inverse sensitivity requires absolute limits; those listed above are used for the tolerance calculations. Additionally, CODE V utilizes 'compensators', or dimensions allowed to vary, to correct for fabrication errors.

The initial setting for the inverse sensitivity analysis of the telescope was an increase of 0.04 λ RMS wavefront error for each of the field angles (0º, 0.35º, and 0.5º). Image plane depth is a standard compensator and its maximum value was set to 0.5 mm in accordance with the thickness of the shim washers between the primary and spacer.
The tolerances calculated for each element are: radius of curvature, axial displacements between elements, tilt angles, cylindrical irregularities, test plate fringes, and radial displacement.

The analysis revealed an increase in error of 0.045 RMS waves or less for each field angle. The cumulative probability for each field angle is shown in Table 1. This probability is based on a 2σ Gaussian distribution.

Table 1. RMS Wavefront Errors

Field Angle	RMS Wavefront Error of the Optical Design	Increase due to Tolerances	Design + Tolerance
0º	0.6228	0.0778	0.7006
0.35º	0.1651	0.1153	0.2804
0.5º	0.7229	0.0865	0.8094

5.3 MATERIALS

The telescope components were rough machined with allowances for final machining on the optical and fiducial surfaces. Each of these surfaces has a minimum of 150μm of extra material that will be removed during final machining. The optical surfaces were compared to their spherical equivalents and the extra sag was added to the 150 μm. The primary has a tapered surface that will press into the tube. It has 150 μm of material plus the taper angle. A photo of the rough machined system is shown in Figure 1.

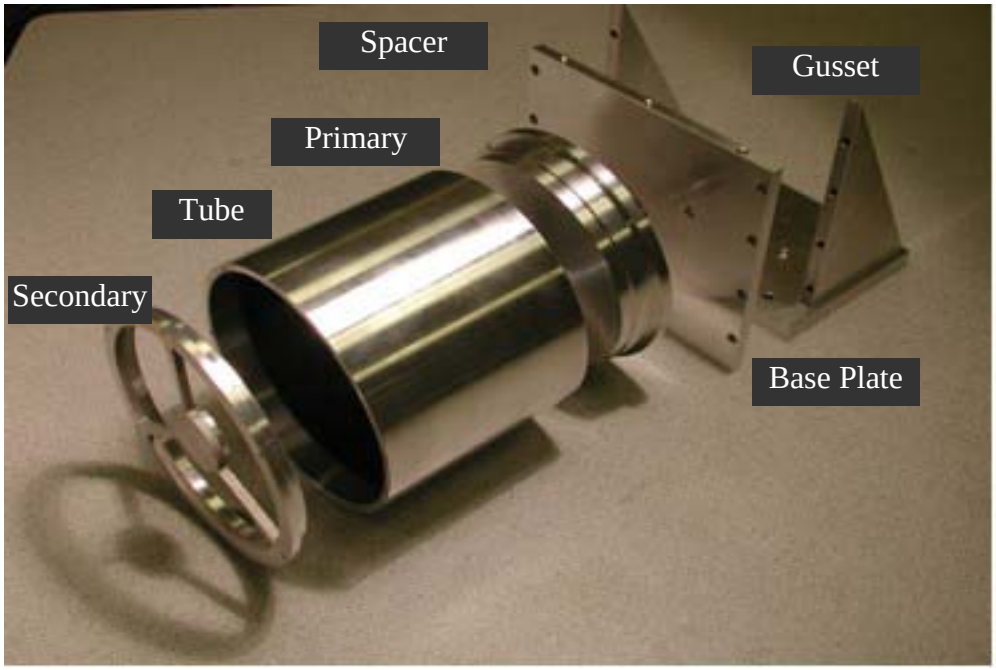

Figure 1. Rough machined components of the two mirror telescope.

To reduce residual stress introduced during the rough machining process, the components were heat-treated. The procedure was as follows:

- Cool the parts to -100º F for one hour at a natural rate, then return to room temperature in a still, ambient atmosphere
- Heat the parts to 300º F at a natural rate for 2 hours and cool in the still, ambient atmosphere
- These two steps are the repeated for one additional cycle.

The stress relief process leads to a reduction in hardness and the original T6 temper will revert to a hardness approaching standard 6061.

5.4 TOOLING

Feed rate and spindle speed are selected based on the desired surface finish, machining time and the characteristics of the spindle. The theoretical surface finish is calculated with a parabolic approximation using the feed rate (f=feed/rev) and the tool radius (R_t) in Equation 1.

$$PV = \frac{f^2}{8R_t} \tag{1}$$

Smaller federates and larger tool radii will improve the finish. However, there is a limit based on the asynchronous vibration of the spindle, the tool sharpness and the material to be machined. Asynchronous spindle vibration will change the tool position from one revolution to the next at any angular position across the face of the part and thus influence the measured finish. The tool edge sharpness will affect the minimum chip thickness and again increase the roughness because it cannot make the chip thickness approach zero. Finally, the material structure (such as the Si in 6061 Al) can create imperfections that will degrade the surface finish.

For the proposed mirror surfaces, a spindle speed of 500 rpm was selected (minimum asynchronous error motion), feed rate of 4 mm/min, a tool nose radius of 5 mm. For this combination the theoretical PV surface roughness will be 1 nm. This surface finish has been created on this machine (1100 Series Al) but not with the 6061 material. The actual surface finish will be on the order of 10 nm RMS due to the issues discussed above.

The DTM x axis table provides room for multiple tool holders. To create both the optical surface and the fiducials in one setup, two tools will be used: a large nose radius (5 mm) allows larger feed rates (shorter machining times) and a “dead sharp” tool can create the steps needed for the fiducials. Both tools will be centered with respect to the spindle axis via standard ogive techniques and the offset between the two will be recorded.

5.5 DIAMOND TURNING PLAN

The diamond turning machine to be used for machining the optical and fiducials is a Rank-Pneumo ASG-2500. It is equipped with hydrostatic oil bearing slide ways with laser interferometer for position feedback (2.5 nm resolution), an air bearing spindle with angular encoder (20,000 point/rev) and a vacuum chuck.

5.5.1 PRIMARY

The primary mirror will be vacuumed to the DTM spindle and the 5 mm nose radius diamond tool will "touch" the chuck surface to set the reference z dimension. The programmed path will be a series of x,z commands that are based on the mathematical description of the hyperbolic optical surface. Because there is a hole in the center of the mirror, a special center plug with o-rings will be used seal the hole. The surface has been roughed machined to a 300 mm radius will be machined to the proper hyperbolic shape with increasing depth until the desired 23.5 mm apex to chuck surface is achieved.

The fiducial feature that transfers the primary optical shape to the secondary is a step on the OD that mates with the tube. The crucial features of this fiducial are the taper angle (1^o), the diameter and the axial distance to the back surface of the mirror. These features will be machined with the "dead sharp" diamond tool and set to z reference by touching off on the vacuum chuck.

5.5.2 SECONDARY

The secondary mirror is another hyperbolic surface but is much smaller (~40 mm diameter) and is convex rather than concave. The optical surface is supported on three arms and has a ring that mates with the other end of the tube from the primary. As with the primary, the optical surface and the fiducial stops are machined on the DTM. To vaccum this mirror to the spindle, a thin plate to seal the area between the outside ring and the optical surface (the thin plate will contact on the support arms).

The space is covered with for the vacuum chuck to work. The machining process for creating the optical and fiducial surfaces is the same as described on the primary mirror above.

5.5.3 TUBE

The tube provides the connection between the primary and secondary mirrors. It sets the axial spacing as well as aligning the two optical axes. The ID of each end includes an radial

interference fit surface with an axial seating surface. These surfaces mate to the primary and the ring on the outside of the secondary respectively. To machine the tube, it will be attached to a flat plate using the 3, #4-40 threaded holes in each end. This plate will be attached to the vacuum chuck and the dead sharp tool will be used to machine the OD and ID. Initially, one end of the tube will be attached to the plate and the axial and radial fiducial surfaces on the ID of the other end will be machined. The distance from the axial stop on the ID and the end surface will be recorded. The exposed end of the tube and a reference surface on the OD will also be machined. The tube will be removed, inverted and reattached to the plate. The OD feature will be used to recenter the tube on the spindle and the surface of the plate will be used as a reference to machine the axial stop of the ID of the other end. This dimension will set the primary/secondary spacing.

5.5.4 SPACER

The spacer will set the distance between the back side of the primary and the camera body. It will be connected to the primary with three machine screws and thin spacers to provide a semi-kinematic mount. The thickness of this spacer will be machined to 25.5 mm by vacuuming it to the chuck and machining with the 5 mm radius diamond tool. This machining step will ensure that the camera will mate squarely and accurately to the system. As reference for both the camera and primary, the machining of this surface provides the most versatile adjustment.

5.6 CONTROLLER PLAN

The hyperbolic surfaces of the primary and secondary mirrors are created with a programmed path that consists of a series of x,z commands. The hyperbolic optical surfaces have a larger radius of curvature at the edges than the center; that is they are flatter at the edges than in the center. Additionally, their sag is less than that of a parabola with an equal base radius thereby allowing use of the parabolic approximation in Equation (1). A 1 nm peak to valley (PV) deviation in height is used to calculate acceptable distance between points (d_p) for the primary mirror in Equation (2). The width of the primary mirror is 62 mm, which yields 1266 x,z points. Employing the same method for the secondary mirror yields 735 x,z points.

$$d_p = \sqrt{(PV) * 8 * R} = \sqrt{(1\text{ nm}) * 8 * 300\text{ mm}} = 48.9\ \mu\text{m} \quad (2)$$

5.7 CONCLUSIONS

Diamond turning multiple optical surfaces is a demanding task and requires attention to detail and careful planning. DTM dynamics and material selection are the main contributions to fabrication induced optical performance decreases.

A 3 mirror telescope is currently being designed. If the off axis conic shapes are needed for this system is needed, a fast tool servo may be needed. In this case the surface must be decomposed into rotationally symmetric and non-rotationally symmetric components that are then cut with the DTM axes and the fast tool servo axis, respectively. The non-rotationally symmetric surface must pass through a mathematical control process named ‘deconvolution’ to correct for the fast tool servo dynamics.

6 MICRO-MACHINING USING ELLIPTICAL VIBRATION-ASSISTED MACHINING

David Brehl
Graduate Student
Alexander Sohn
Precision Engineering Center Staff
Thomas Dow
Professor
Department of Mechanical and Aerospace Engineering

6.1 INTRODUCTION

"Elliptical Vibration-Assisted Machining" (EVAM) uses two parallel piezoelectric actuators to drive a single-crystal diamond cutting tool in a cyclical path. By exciting the piezo stacks with sinusoidal voltage signals, with the rake face cycle leading that of the clearance face by 90 degrees, the tool can be driven through an elliptical path (Figure 1). During each elliptical pass of the tool, the path advances in the upfeed direction relative to the workpiece, due to the feed motion of the work. As a result, successive passes of the tool overlap. EVAM avoids problems of tool deflection, chatter, runout, and vibration associated with other chip-making processes like micro-milling. It can also achieve cut edges which are virtually burr-free. Finally, because the tool is cutting in the workpiece for only part of each elliptical cycle, average cutting forces, and the opportunity for tool wear from mechanical or chemical effects, are reduced when compared to conventional machining.

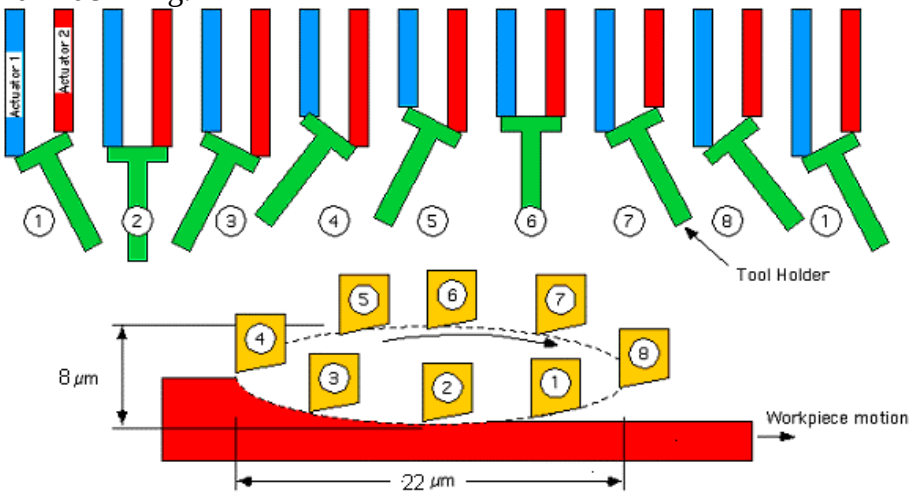

Figure 1. EVAM Using 2 Piezoelectric Actuators

6.2 EXPERIMENTAL SETUP

Figure 2 shows a cutaway view of the Ultramill, an EVAM tool built by the Precision Engineering Center. The two piezoelectric actuator stacks are located in a closed chamber through which a dielectric coolant circulates continuously. A titanium diaphragm applies preload to the piezo stacks and seals the coolant in the chamber.

For raster machining experiments, the Ultramill is installed on the PEC's Nanoform 3-axis diamond turning machine (DTM). The workpiece is held in place by a vacuum chuck. A 20x-140x zoom videomicroscope is used to monitor tool tip position for determining touchoff.

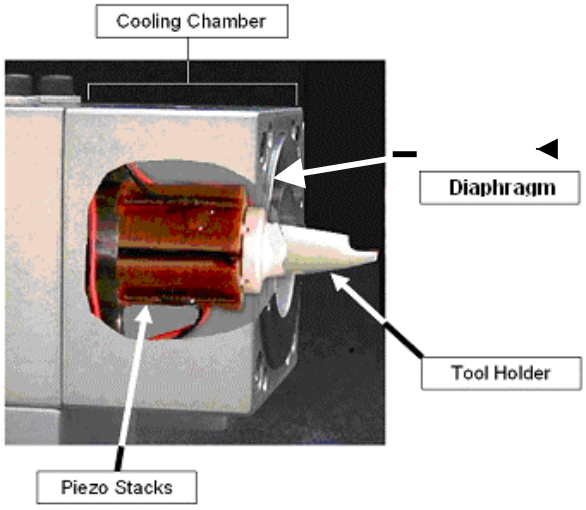

Figure 2. Cutaway view of the Ultramill

6.2.1 STAINLESS STEEL MACHINING

Machining of stainless and tool steels is an important area of interest for EVAM, because these materials can be used to make molds and dies for micro-molding and micro-embossing applications. As an initial step, the Ultramill was used to machine a binary feature (Figure 3) in annealed 17-4 PH stainless steel. This demonstration part is a "thunderbird", adapted from the logo of Sandia National Laboratory. The part was cut using a tool with 1 mm nose radius; the tool was freshly lapped for stainless steel experiments. The overall size of the background on this part is 1.2 x 1.2 mm. The flat background is cut 2 μm below the surrounding material surface, and the raised thunderbird itself is 1 μm tall relative to the background. Surface finish in both upfeed and crossfeed direction is approximately 20 nm RMS.

Unlike most parts made by the Ultramill, the surface of the stainless steel workpiece was not pre-machined to an optical surface, but was only surface ground. Touchoff was more difficult because the reflection of the tool in the workpiece was diffuse, making it difficult to establish when the tool tip initially contacted the work surface. To uncouple machining of the part from the need for a precision touchoff, the machining program had 2 stages. First, a flat area was machined in the workpiece surface, to provide a plane of constant depth into which the actual part could be machined. Then the part itself (consisting of a recessed background and raised

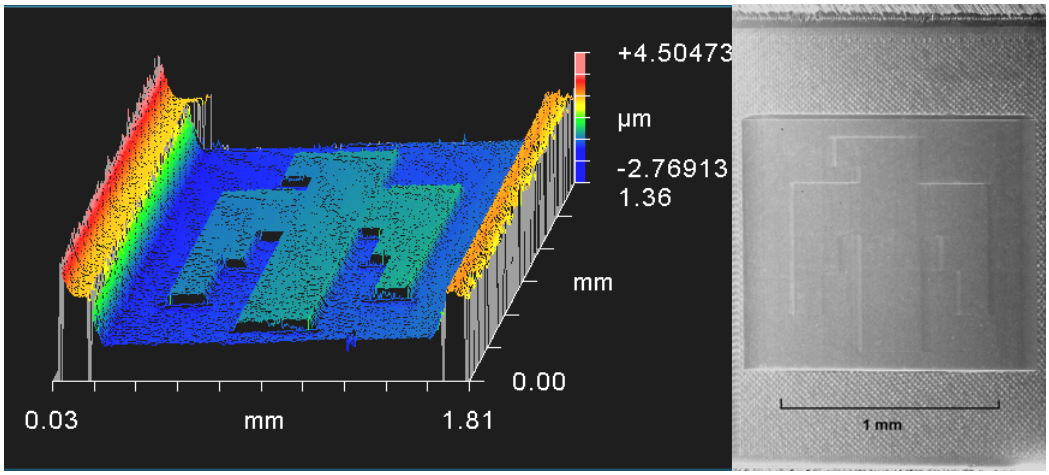

a) Interferogram b) SEM Image

Figure 3. Thunderbird Machined in 17-4PH Stainless Steel

feature) was cut, using the flat machined area as a datum in the Z (depth) direction. The initially-cut area appears in Figure 3b as a "diamond plate" texture, while the raised thunderbird and background present a "smooth" appearance. This is because the flat area was machined using a different set of cutting parameters (upfeed velocity and crossfeed increment) than the actual part. While this was done mainly to minimize the overall machining time for the part, it also shows the capability of the Ultramill to create arbitrary finishes and textures in a surface.

SEM images of the 1 mm radius tool were taken before and after machining a series of three parts. At this point the tool had accumulated 1.2 m total cutting distance, with no discernable wear.

6.2.2 High Relief Features

Raster machining requires multiple (in some cases, several hundred) upfeed (X-direction) passes, with the tool stepped incrementally in the cross-feed direction (Y-direction) between upfeed passes. However, most of the parts made by the Ultramill to date have only required a single "cut"—the maximum depth of cut (Z-direction) and all features in the Z-direction are obtained by a single series of raster passes. The tool is never returned to the X-Y origin to make additional, deeper, machining passes over regions, which have already been cut.

More complex structures might need to be fabricated using multiple cuts in the Z-direction, in which the tool makes repeated series of raster passes at successively greater depths. Such structures include microfluidics applications requiring deep pockets or channels, and geometries which have variable cross sections in the Z direction.

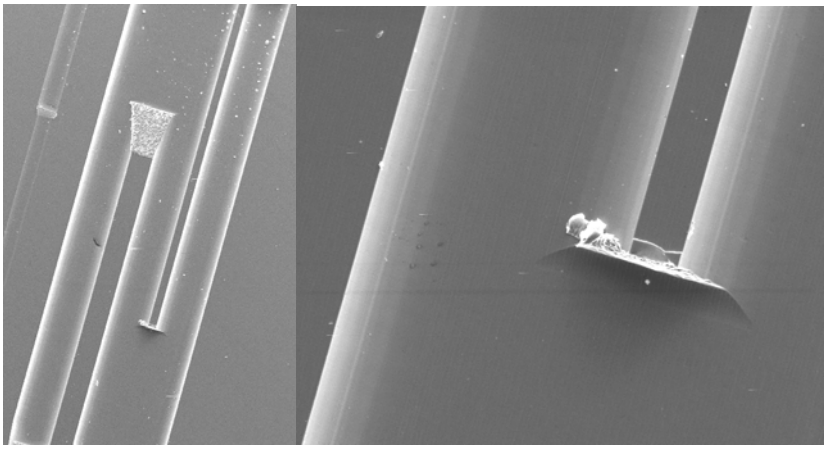

a) Overall Part b) Detail of ridge headwall

Figure 4. Ridge-and-Channel Part, 20 μm Maximum Height Differential

Several parts have been made using multiple Z-direction cuts. These include the ridge and channel structure shown in Figure 4. Figure 4a is an SEM image of the overall structure. It was cut in copper using a tool with 50 μm nose radius. This part has a 20 μm height differential between the ridge tops and deepest part of the adjacent channels. It was made by making 4 successive series of raster passes, each 5 μm deep. This part has the largest differential height made to date. Figure 4b is a detail of the part in Figure 4a, and shows characteristics common to all the parts made in this set of tests. Because of the tool nose radius, the side walls of the channels have a 50 μm radius which also sets the minimum crossfeed spacing between ridges (this limitation can be overcome by using a tool with sharper nose radius, or with a square nose profile). The headwall, formed in the upfeed direction, is near-vertical and is visually smooth. The wall on the adjacent ridge, formed in the trailing direction relative to tool upfeed motion, is a 10-degree ramp deriving from the clearance angle of the tool. The clearance face of the tool impacting the work surface during the initial plunge to cutting depth on each series of raster passes caused the pebbled finish of this ramp. The tool should have been programmed to make a simultaneous move in Z and X, to keep the tool moving parallel to the portion of the ridge created by the preceding set of cuts. The sharp headwall and ramped trailing wall are characteristic of what can be achieved with the Ultramill in the present 3-axis raster machining mode. This limitation can be overcome with 4-axis machining—by changing the part orientation relative to the Ultramill's feed direction, all walls can made on the upfeed side of the machining ellipse, and would be like the headwall in Figure 4b.

The sides of the ridges and channels show near-zero burr. Burring and damage is visible at the top of the headwall. This is believed to be the result of selection of machining parameters. The DOC on this part was larger than the semi-minor axis of the machining ellipse. This condition

causes continuous chips to be produced, which break off from the workpiece, leaving a burred or irregular edge.

6.2.3 AXIS VIBRATION ANALYSIS

The effect of axis vibration on surface finish of parts made by the Ultramill has been explored. [1] In particular the vibration response in the Z-direction was investigated for the Nanoform's X-, Y-, and Z-axes, and the locked spindle holding the vacuum chuck. A mechanical shaker was used to impart a known oscillatory motion to each axis, and the Z-direction response of the system was measured using the DTM's position-feedback interferometers. FFT analysis was applied to the system response. Table 1 reports the 2 frequencies with the greatest displacement amplitude, and the associated peak displacement, for each axis. It is seen that the Z-axis, X-axis, and spindle amplitudes are much smaller than those of the Y-axis. Also the frequencies with the greatest amplitude for the Y-axis and Z-axis are similar, 95 and 102 Hz. Finally, the second largest amplitude response for the Z-axis is of the same magnitude as the peak displacement amplitude for the X-axis.

Table 1: Nanoform Axis Resonant Frequencies and Associated Displacments

		Resonant Frequency (1st)	**Displacement Amplitude**	**Resonant Frequency (2nd)**	**Displacement Amplitude**
Axis	**Direction**	Hz	μm	Hz	μm
X	X	120	0.1		
	Z	275	0.01		
Y	Z	95	8.2	50	1.9
Z	Z	102	1.8	70	0.33
Spindle	X	300	0.1		
	Z	190	0.01		

Flats were machined and the spatial frequency determined for surface profiles along the upfeed direction. The component frequencies were found using FFT, and compared to the axis response frequencies from the shaker tests. The 2 frequencies associated with greatest feature size in the part were 100 Hz and 60 Hz. These are very close to the Z-direction resonant frequencies determined for the Y- and Z-axes. It is theorized that vibration of the Y- and Z-axes, in some combination, is therefore responsible for much of the surface roughness beyond the theoretical finish from upfeed and crossfeed, found in parts machined to date.

6.3 CONCLUSIONS

The Ultramill is capable of creating binary features in stainless steel, with surface finishes of 20 nm RMS or better.

Structures have been created with height differentials of up to 20 μm between adjacent features. Smooth feature sides and walls can be achieved. Proper selection of values for process variables (DOC vs machining ellipse dimensions) is important to avoid burring-type damage to edges perpendicular to the upfeed direction.

Z-direction vibration of the current Y-axis appears to be responsible for much of the surface roughness (beyond the predicted theoretical finishes) seen in parts made to date. A new Y-axis has been ordered from Moore Nanotechnology Systems (Keene, NH) with delivery estimated by mid-August 2005. The new Y-axis will have significantly greater stiffness in the Z-direction: approximately 2.0 MN/m, compared with 0.5 MN/m for the present Y-axis. This is expected to reduce the amplitude of Z-direction vibration of the Y-axis, with corresponding potential improvement in surface finish.

Other future work includes evaluating tool wear after machining in stainless steel for extended cumulative distances (100 meters or more). Development of 4-axis machining procedures on the Nanoform is needed in order to make parts with arbitrary 3-D geometries, without limitations imposed by the shallow angle caused by the tool clearance face.

REFERENCE

1. Brocato, B., “Micromachining Using Elliptical Vibration Machining”, MS Thesis, North Carolina State University, 2005

ACKNOWLEDGEMENTS

This project was funded in part by the National Science Foundation under contract DMI-#0423315, monitored by G. Hazelrigg.

Stainless steel machining activity was funded in part by Sandia National Laboratory.

7 TEM AND RAMAN SPECTROSCOPIC ANALYSIS OF SINGLE POINT DIAMOND TURNED SILICON

Timothy Kennedy
Graduate Student
Ronald Scattergood
Professor
Department of Materials Science and Engineering

7.1 INTRODUCTION

Diamond turning and parallel flycuts were performed on (100) Si along the <011> direction using both -30° and -45° diamond tools with feedrates falling with in a 1 to 15 µm/rev range. All samples were analyzed with both micro and macro Raman, and preliminary cross sectional TEM has been completed on the 1 and 5 µm/rev samples. A correlation between the Raman spectra and cross sectional TEM images of the diamond turned silicon will be attempted. Dislocation loops and slip planes were found at depths up to 250 nm below the surface of both feedrates; along with a previously unseen structure below the amorphous layer. Flycut samples were machined with two separate set of tools, and it was found that depending on tool edge design an amorphous layer was not always created. TEM analysis is still needed to analyze subsurface damage, and to determine the deformation mode (i.e. high pressure phase transformation (HPPT) or dislocation movement).

7.2 PROJECT DETAILS

For this project TEM and Raman data were collected from (100) oriented silicon that was diamond point turned along the <110> type direction. Different crystal orientations are available but it has been shown that (100) oriented silicon provides the best ductility [1]. Samples were machined using a traditional diamond turning setup and a parallel fly cutting technique the latter using two sets of tools consisting of a -30° and -45° rake angle round nose diamond tool.

7.2.1 EXPERIMENTAL SETUP

A Rank Pneumo ASG 2500 Diamond Turning Machine was used to create the samples for this study. The fly cutting samples were 1 cm wide by 2 cm long, and are oriented so that the cutting direction follows the <110> type direction across the 1 cm width; as compared to an entire wafer for the traditional setup. The tools used were round nosed diamond with rake angles of -30° and

-45°. Two diamond turning setups were used; the first a traditional lathe setup and the next a parallel fly cutting setup. Unlike the traditional lathe setup where the tool is on the x-axis and the sample in on the spindle; parallel fly cutting has the tool on the spindle while the sample is on the x axis parallel to the tool so that a flat cut can be made. Since carbon reacts with silicon, the latter technique reduces the diamond tool wear since the diamond is not always in contact with the silicon.

The parameters used during turning have an effect on the amount of back transformed a-Si [2]. At slower feed rates, the more amorphous material is formed. Therefore, spindle speed and feed rate need to be optimized so that the layered structure can be controlled through machining, instead of other processes such as thermal annealing. But it has also been shown that tool geometry has a great effect on subsurface layers [3]. A straight nose tool produces the opposite that is observed with a round nose tool. Samples have been prepared with feed rates between 15 and 1 μm/rev. Surface finishes of the ductile-turned regions were measured using a Zygo New View 5600 white light interferometer. Once the surface finish was evaluated samples were analyzed with Raman spectroscopy and TEM.

7.2.2 EXPERIMENTAL RESULTS: TRADITIONAL SETUP

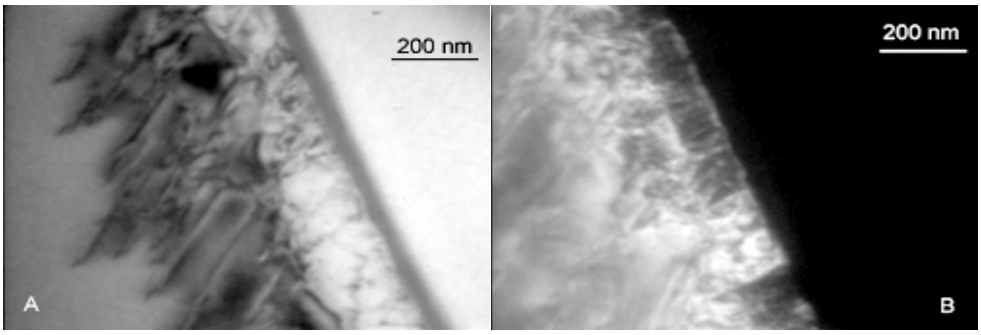

Figure 1. Bright Field (A) and Dark Field (B) pair, 199,000x, 1 μm/rev

The Bright Field/Dark Field pair in Figure 1 shows dislocation structures, and what looks to be a columnar layer (1b). The 5 μm/rev sample in Figure 2 illustrates dislocation loop structures. Also through weak beam imaging, a columnar structure is visible at the higher feedrate (2c). The conventional TEM image in Figure 3 indicates {111} slip planes and evidence of dislocation loops. Figures 1, 2, and 3 all show an amorphous layer as predicted by the Raman spectra in Figure 5 since the characteristic peak at 470 cm^{-1} for amorphous Si can be seen. Average layer thickness differs only by 4.5 nm, and is statistically insignificant as shown by the range of values in Figure 4. The lack of a discernable difference in the a-Si layer depth does not follow the trend set forth by the Raman spectra Figure 5. The columnar structure seen in Figures 1b and 2c are an actual dislocation structure since no polycrystalline diffraction pattern could be found.

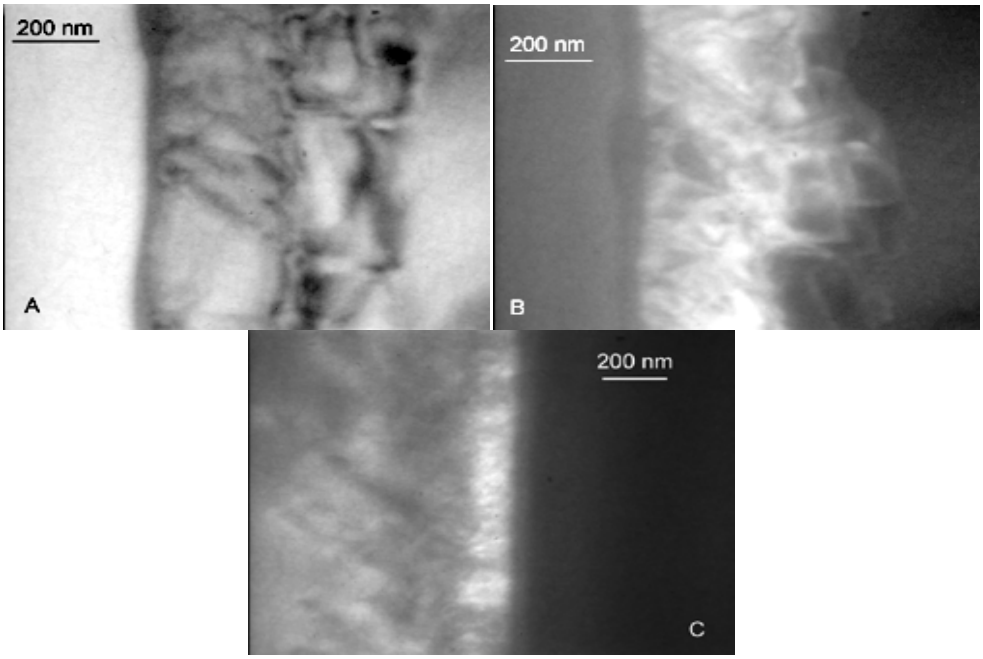

Figure 2. Bright Field (A), Dark Field (B) pair 199,000x, (C) Weak Beam DF 157,000x 5 μm/rev

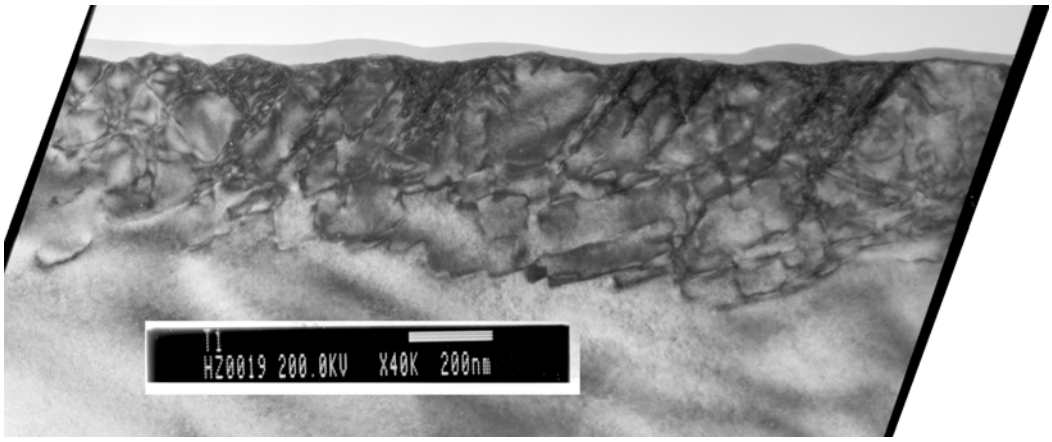

Figure 3. Conventional TEM image, 40,000x, 5 μm/rev.

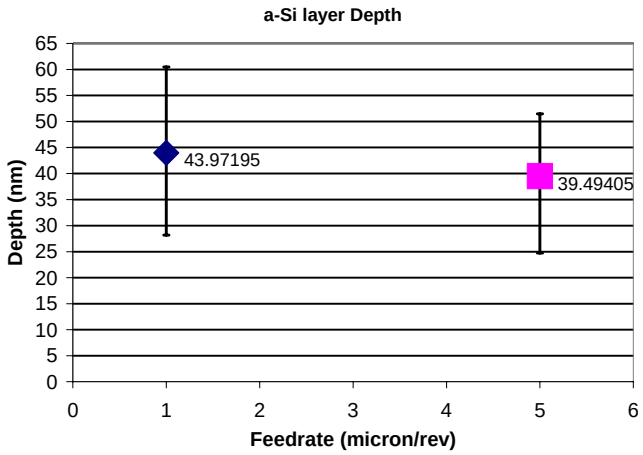

Figure 4. a-Si layer depth versus federate.

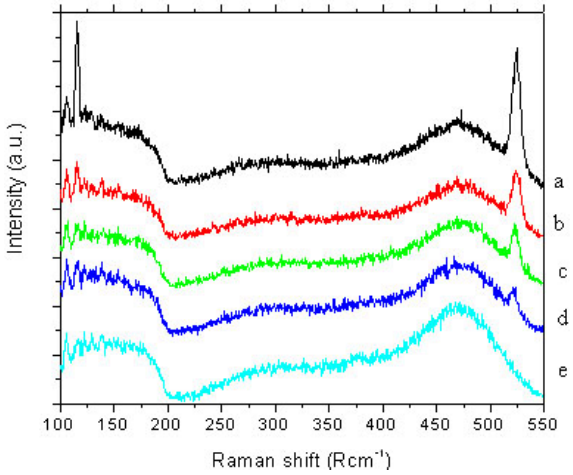

Figure 5. Raman spectra at feed rates a) 15, b) 7, c) 3, d) 2, and e) 1 μm/rev. [1]

7.2.3 EXPERIMENTAL RESULTS: PARALLEL FLY CUTTING

At this time only Raman data has been recorded for the parallel fly cut samples. As previously mentioned the fly cut samples were machined using two separate sets of tools, with different cutting edge designs. This difference has an impact on the subsurface structure created as shown in the Raman spectra. Due to unforeseen events the old -30° tool and the new -45 ° tool were unable to be used in this experiment. Figure 6 shows the spectra of a sample cut with a newer -30° tool, note the absence of a-Si at 470 cm^{-1}. The old -45 ° tool however was able to reproduce the original data, Figure 7 is the spectrum from the parallel fly cutting and Figure 8 is the spectra from the traditional lathe setup. Both showing a small a- Si peak at 470 cm^{-1}.

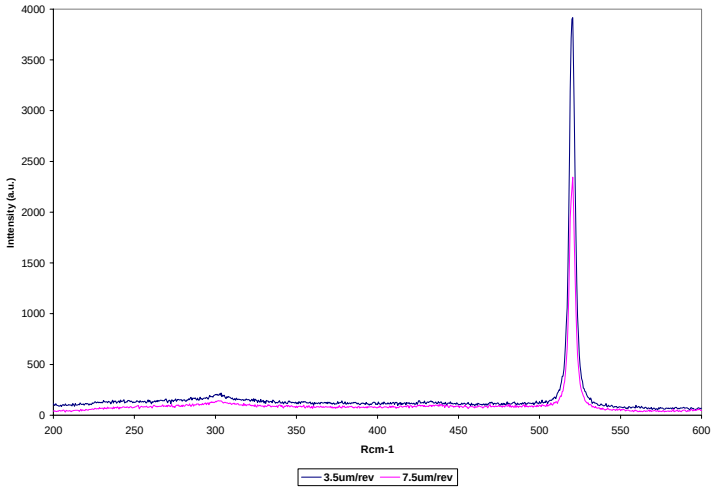

Figure 6. Raman data showing no a-Si at 3.5 and 7.5 μm/rev.

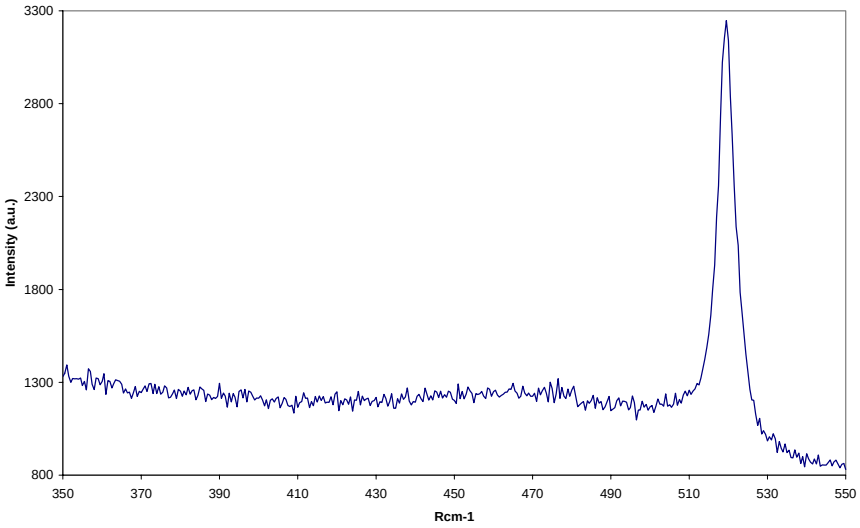

Figure 7. 1 μm/rev Raman spectrum from the old -45 ° tool on the parallel fly cutter

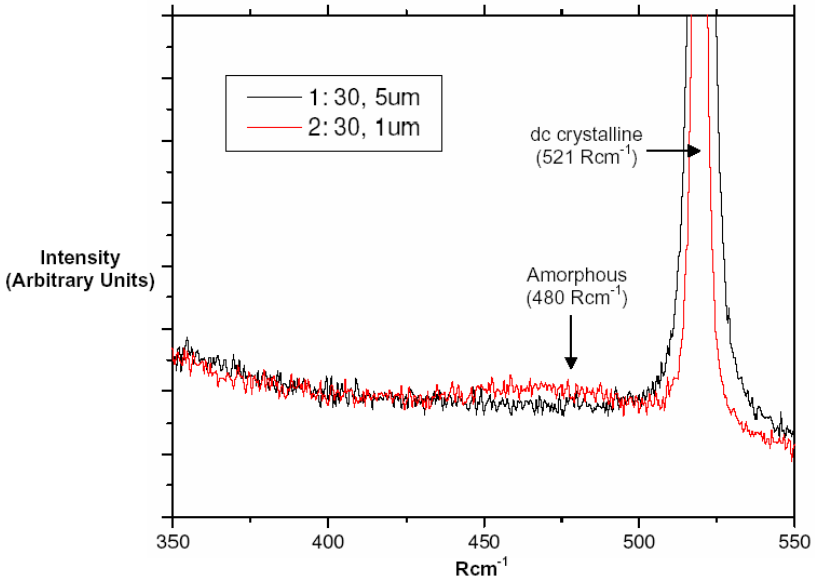

Figure 8. -45 ° tool Raman spectra on the traditional DTM setup [1]

The question that arises from the TEM images and Raman spectra is if a High Pressure Phase Transformation (HPPT) actually occurs. Other groups have reported dislocations, dislocation loops, and slip planes but no one has viewed the columnar structures in Figure 1b and 2c [4, 5]. If an HPPT is occurring then the loops and slips planes indicate a normal metallic deformation mode when the silicon transforms into ductile Si-II. This does not explain the presence of the columnar structure, which is perpendicular to the amorphous layer. Such a layer possibly indicates a melt zone at the surface or some other unexplained phenomenon. Another point is the existence of the amorphous layer. Once again there is evidence for either an HPPT or other deformation mode. The theory in silicon HPPT is that upon unloading the Si-II will back transform through various phases until it reaches the amorphous stage, at which time it does not have enough energy to recrystallize into Si-I leaving a metastable a-Si, as illustrated in Figure 9. If viewed through a traditional deformation mode, the amorphous layer exists due solely to the extreme high pressure at the surface under the diamond tool, and the dislocations underneath follow traditional silicon slip mechanisms. More in depth studies will need to be performed to pin point the true deformation mechanism.

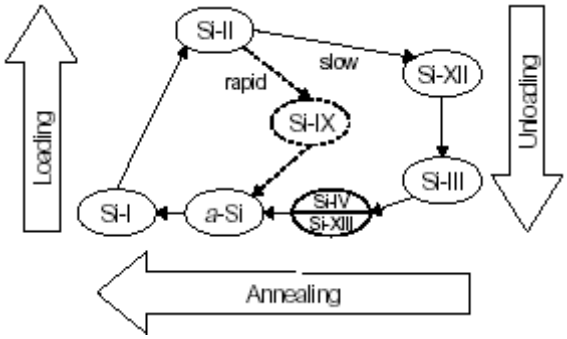

Figure 9. Si transformation schedule [2]

7.3 CONCLUSIONS

From the TEM and Raman data it is clear that the back transformed material contains an amorphous layer and a deeper damage layer. Multiple research groups have also seen this structure, but it is important to note that no in depth evaluation of the damage layer before. When the Raman spectra and TEM images are compared, the qualitative comparison is poor since there is no statistical difference in layer thicknesses. There is a very thin amorphous layer compared to the rest of the image. At this point, the existence of an HPPT in silicon during diamond turning is still questionable, and any mode or mechanisms set forth are only theoretical. To determine whether or not silicon undergoes an HPPT, more samples at various feedrates need to be created and analyzed though both TEM and Raman spectroscopy both in cross section and plan view.

7.4 FUTURE WORK

More silicon samples need to be machined at different feed rates and with different machining techniques. These samples will then be examined with Raman and TEM. Scanning electron microscopy (SEM) will be explored to view the cutting edge of the different tools.

REFERENCES

1. Randall, T., M.S. Thesis, *Characterizing the Ductile Response of Brittle Semiconductors to Dynamic Contact Processes*, North Carolina State University, 2004. http://www.lib.ncsu.edu/theses/available/etd-06182004-104005/

2. Domnich, V. and Y. Gogotsi. “Phase Transformations in Silicon Under Contact Loading”, Rev. Adv. Mater. Sci. 3(2002) 1-36

3. Yan, J. “Laser micro-Raman spectroscopy of single-point diamond machined silicon substrates”. J. App. Phys. Vol. 94 Number 4 (2004) 2094-2101

4 Shibata, T. “Cross-section transmission electron microscope observations of diamond-turned single-crystal Si surfaces”. Appl. Phys. Lett. 65 (20), 14 November 1994. 2553

5. Kunz, R. “High Resolution studies of crystalline damge induced by lapping and single-point diamond machining of Si(100)”. J. Mater. Res., Vol. 11, No. 5, May 1996. 1228

8 METROLOGY OF REFLECTIVE OPTICAL SYSTEMS

Robert Woodside
Graduate Student
Thomas Dow
Professor
Department of Mechanical and Aerospace Engineering

8.1 INTRODUCTION

The goal of this research is to develop techniques for measuring the performance of an optical system. These systems consist of a number of optical surfaces that must be independently fabricated with fiducial features that allow them to be assembled into a system. The emphasis on the design and fabrication tasks has been on reflective systems but some effort has also been dedicated to refractive systems. The reflective surfaces must be measured individually to see show the fidelity of the shape compared to the design dimensions. In addition, the relationship between the optical surface and the fiducial features must be determined. Therefore, this project involves measurements of individual components with profilometer, interferometer and Coordinate Measuring Machine (CMM) techniques as well as systems using dual pass interferometers and CMOS array images.

8.2 COMPONENT MEASUREMENTS

Metrology of the individual optical elements and fiducial surfaces for the Richey Telescope will be measured using the contacting profilometer and CMM. Two profilometers will be used for the measurement, one using rectangular coordinates and one with polar coordinates. In addition, the CMM will be used to assess the relative location of the optical surfaces and the fiducial elements.

8.2.1 TALYSURF TECHNIQUES

The Talysurf profilometer, as shown in Figure 1, consists of a contacting probe on a pivoted arm that is supported on a square reference bar. The vertical motion of the probe as it moves along the bar provides a measurement of the shape and surface finish of the surface. A laser interferometer is used to sense the vertical motion of the probe. For the secondary mirror shown in Figure 1, the surface is crowned in the lateral direction to find the high spot and then a linear measurement of the surface is made. The mirror is rotated, again crowned and a second trace is made. A number of these traces can be assembled to create 3D image of the surface.

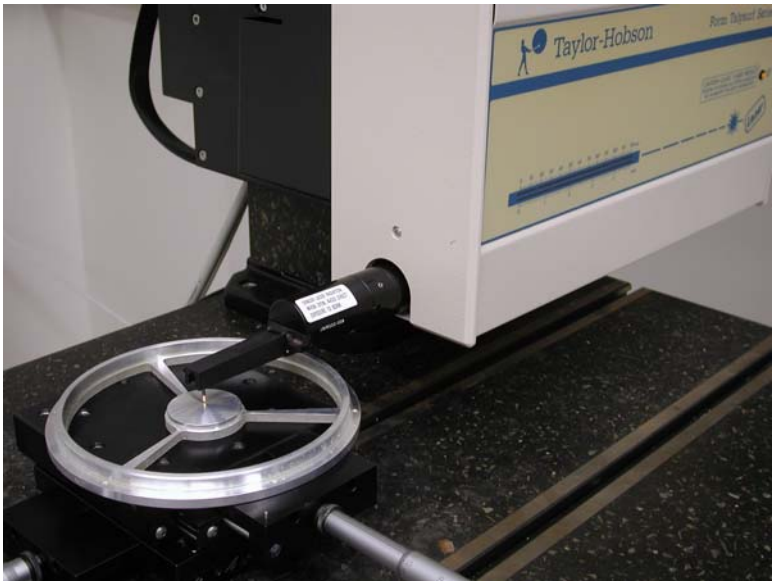

Figure 1. Taylor-Hobson Talysurf Profilometer with secondary mirror

The profilometer has an advantage over optical instruments because the measured surface does not need to be reflective. However, the disadvantage is that the probe contacts the surface and can damage it. In addition, for the small slopes present in the primary and secondary mirrors, the crowing process may create uncertainty in the location of the center and therefore the relative orientation of the different traces measured. The range of motion of the Talysurf in the horizontal direction is 120 mm (resolution of 20 μm) and in the vertical direction is 6 mm (resolution of 10 nm). A longer probe is available that doubles the vertical range but cuts the resolution in half.

8.2.2 POLARIS POLAR PROFILOMETER

A second profilometer available at the PEC uses polar coordinates rather than the x-y system of the Talysurf. The primary advantage of polar coordinates is to keep the probe tip orthogonal to part being measured. This allows optical surfaces with more curvature and a larger angular range to be measured. The Polaris machine shown in Figure 2 consists of a motor driven, air-bearing rotary stage with a linear stage mounted on top. An air-bearing capacitance gage is mounted on the linear stage and contacts the surface to be measured. The part is mounted on the vacuum chuck which has x-y-z positioning stage to locate the part with respect to the rotary axis prior to measurement.

The first version of Polaris used the part program to drive the r and θ axes and the capacitance gage recorded the deviation from that desired part shape. To make the system easier to use, the Polaris is being modified to follow the part profile by using feedback from the capacitance gage to drive the r axis and keep the capacitance gage within its 50 μm range. With this control scheme, any arbitrary shaped part can be measured with minimum operator interaction.

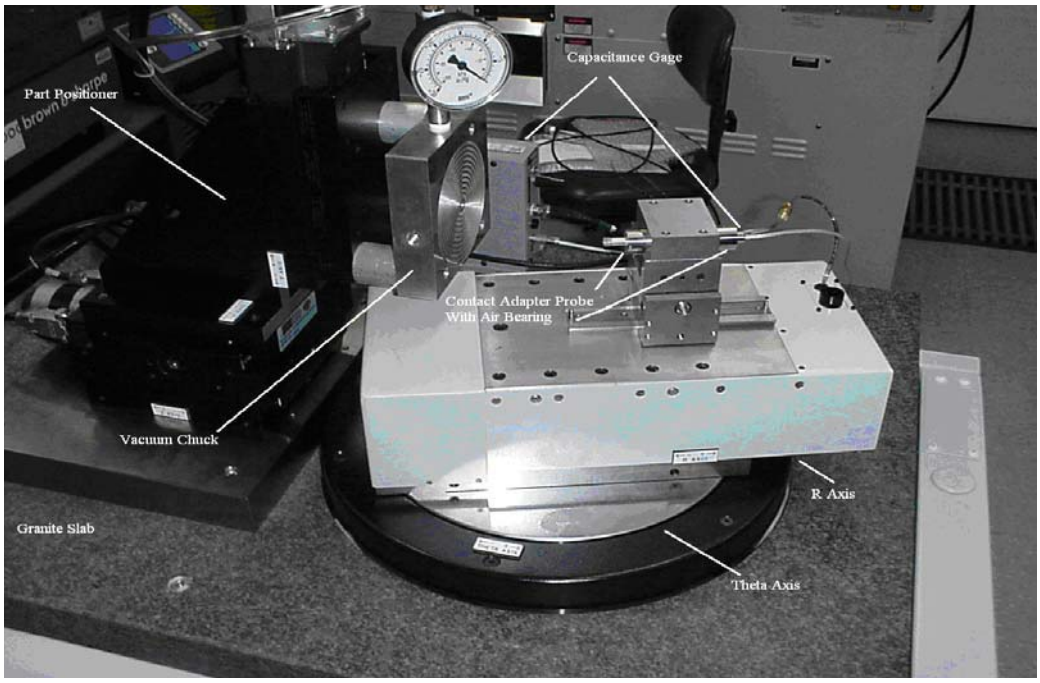

Figure 2. Polaris Polar Profilometer – get another picture with a part on the vac chuck – use bigger font on the labels

This modification requires intricate knowledge of the dynamics of the r and θ axes as well as the air-bearing capacitance gage. The control system must be designed so that the r axis follows the probe without becoming unstable or allowing the probe to go out of range. A DeltaTau PMAC system is used to control the Polaris axes and read the positions for a coordinate measurement. The dynamic characteristics of each axis are being determined and a user interface to allow measurements of optical surfaces is being created.

8.3 OPTICAL SYSTEM MEASUREMENT

The shape of the individual components must give way to system performance measurements once the components are assembled. Several techniques are being evaluated to provide a measur ement of the system.

8.3.1 DUAL-PASS INTERFEROMETER

The entire optical system will be tested using a double-pass interferometer. The telescope will be mounted on a linear/tilt stage on the intermediate stage of a Zygo GPI interferometer shown in Figure 3. A spherical wavefront will be focused on the detector plane above the back of the primary mirror. A narrow spherical mirror surface machined on the ID of the hole in the primary will be used to center the telescope in the GPI beam. Because the detector plane is at the focus of the secondary mirror, the light from the interferometer will be reflected onto the primary mirror and produce a linear wavefront out of the front of the telescope. A flat reflector, also on a tip/tilt stage, will be placed on the bottom to reflect the light back through the telescope and into the interferometer as illustrated in Figure 4. A perfect telescope and reflector will generate no fringe patterns in the interferometer.

Figure 3. Zygo GPI used for dual-pass interferometer measurements

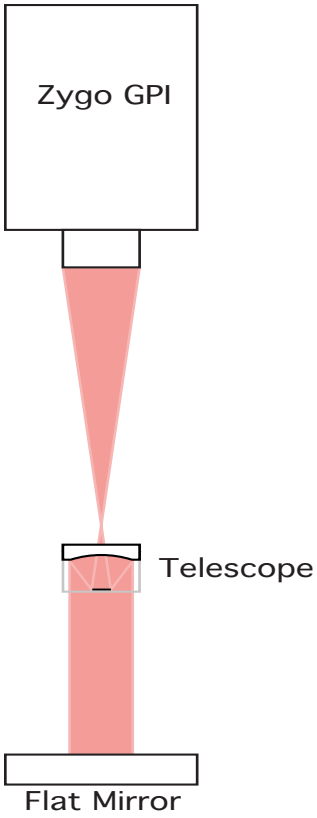

Figure 4. Double-pass interferometer setup for measuring optical system

The dual pass interferometer will allow the complete telescope to be measured including the shape and the location of the mirrors. Errors in either will show up as a wavefront error in the interferogram. By creating synthetic interferograms for the expected errors in the telescope (for example wavefront errors at different field angles shown in Figure 5), the system performance can be measured and an estimate of the error source can be determined. To measure the performance at different field angles, the telescope in Figure 4 is laterally shifted and the flat mirror at the bottom is tilted to the off-axis locations shown in Figure 5.

Other specific fabrication errors can also be evaluated by forcing misalignment of one component with respect to another. For example, the secondary mirror can be moved axially and the interference image can be predicted in Code V and measured in the dual-pass interferometer. Possible methods for translating the secondary mirror include hanging small weights and inserting a screw from the side to push on the mirror. Each of these methods will produce known deflections that can be used to produce off-axis rays comparable to those produced in the Code V software. The software on the Zygo GPI (MetroPro) can also create Modulation Transfer Functions, Point Spread Function and general wavefront error plots. Code V produces similar

plots and the two can be compared. Code V can also create plots for both on and off-axis beams as illustrated in Figure 5. These expected shape can be compared to the measurements for the tilted telescope discussed above to obtain a full characterization of the optical system. The wavefront error data can also be inserted directly into the Code V software to produce a reference surface. This imported surface can be compared against the expected surface produced by Code V to derive the experimental error.

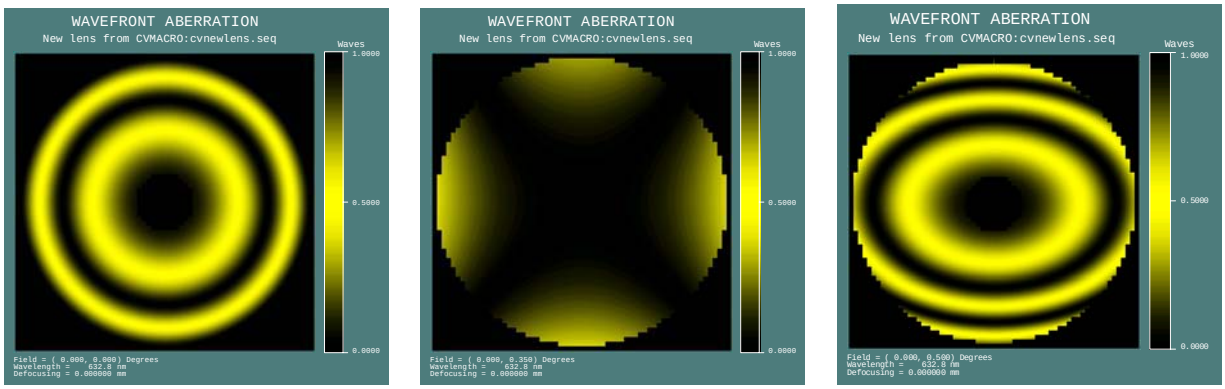

Figure 5. Interference patterns at three field angles: center (left), 0.35º (middle) and 0.5º (right)

8.4 CONCLUSIONS

Metrology of the individual telescope components as well as the assembled system provides important information relating the design process to the system performance. The research area addressed here involves techniques for component and system evaluation. Linear and polar profilometers are used to measure the shape of the optical surfaces created and system performance is measured using a dual-pass interferometer arrangement.

Future work will refine these processes. Application of the techniques for off-axis conics and freeform surfaces will be addressed and changes to the Polaris machine to allow probe following will be made. A rotary table will be added to the Talysurf to assist in the orientating multiple measurements.

9 NON-CONTACT TRANSPORTATION USING FLEXURAL ULTRASONIC WAVE

Yanbo Yin
Graduate Student
Paul I. Ro
Professor
Department of Mechanical and Aerospace Engineering

9.1 INTRODUCTION

In manufacturing and processing precision products such as compact discs, LCD, LSI and silicon wafers of semiconductors, a non-contact transportation system is indispensable to eliminate tiny defects and scratches. In order to realize such a system, several techniques have been proposed, e.g. gas bearing: transportation with an electromagnetic force or a static electronic force. In these systems, however, several problems must be overcome: (1) Levitated objects are constrained to electrically conductive materials except the gas bearing. (2) In the gas bearing systems, not only an abundance of gas is needed, but also the levitation and transportation mechanism is too complicated and expensive to be conducted. Acoustic levitation can be employed in a non-contact transportation system due to the following advantages: (1) no materials type limited to the levitated object, (2) compact size, (3) free of noise and (4) no demand on large amount of clean gas. This project conducted in PEC first investigated acoustic levitation, designed the experiment setup, proposed governing equations of acoustic levitation and checked the validity. In this report, the experiment setup for the transportation system is described and the performance of the system is investigated.

9.2 DETAILS OF THE PROJECT

9.2.1 NEAR FIELD ACOUSTIC LEVITATION (NFAL)

The relationship between levitation and input voltage is shown in Figure 1 where it can be seen that the levitation distance is proportional to the amplitude. The top two lines represent the levitation of two objects with different mass but same mass area ratio.

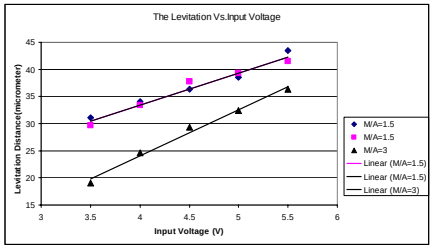

Figure 1. Levitation vs. Input Voltage

Experiment Set-up

The experiment was carried out using the conFigureuration shown in Figure 2. It consists of one rectangular vibration plate (54*40*3 mm) and one mechanical horn connected to the Piezo actuator.

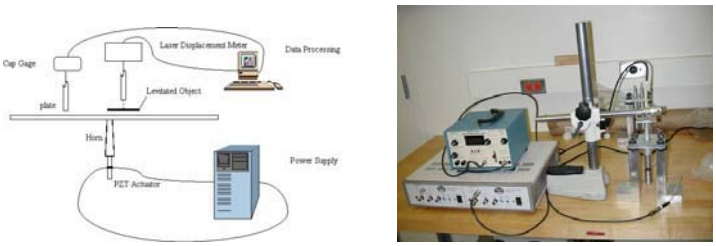

Figure 2. Experimental Set-up

The actuator was Bolted Langevin type Transducer (BLT) manufactured by NTK (Model No. DA2228). The levitated object was placed on the surface of the rectangular plate which was excited at frequency of 16.8 kHz. The vibration amplitude measurement was conducted by a Capacitance Gage and the levitation distance by laser displacement meter (Angstrom Resolver Model 101), respectively. Aluminum was chosen as the material of horn and beam because of its excellent acoustic characteristics.

Analytical Approach

Levitation by flexural vibration Consider that a plate vibrates in the flexural mode and a planar object is levitated by a distance of h as shown in Figure 3. In this case, the acoustic wave does not propagate normal to vibrating source. The particle velocity amplitude distribution can be derived as the sum of plane waves [2]:

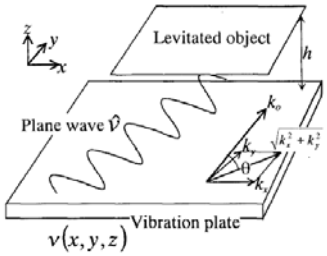

Figure 3. Scheme of Levitation by flexural vibration

$$v(x,y,z) = \frac{1}{4\pi^2}\iint \hat{v}(k_x,k_y)\times \exp[\,j(k_x x + k_y y + k_z z)]dk_x dk_y \tag{1}$$

Where:

$$k_x^2 + k_y^2 + k_z^2 = k_a^2 = (\omega/c)^2 \tag{2}$$

For a plane wave, it has two wave vectors: k_x, k_y, the radiation pressure in the z direction is derived as:

$$P(k_x,k_y) = \frac{1+\gamma}{2}[1+\frac{\sin(2k_z h)}{2k_z h}] < E_z(k_x,k_y) > \tag{3}$$

Where:

$$< E_z(k_x,k_y) >= \frac{\rho_a \hat{v}^2(k_x,k_y)}{4\sin^2 k_z h} \tag{4}$$

The total radiation pressure in z direction can be the sum of each vector component and given as:

$$P\big|_{z=h} = \iint\limits_{k_x^2+k_y^2<k_a^2} P(k_x,k_y)dk_x dk_y \tag{5}$$

9.2.2 ULTRASONIC TRANSPORTATION

Figure 4 shows the schematic diagram of the non-contact transportation system using flexural traveling wave. The traveling wave sound source produces two unidirectional forces on the object in the gap. One is in the normal direction and levitates the object and the other induces the near boundary streaming in the parallel direction. The velocity gradient of the near boundary streaming on the surface of the object produces the viscous force that causes the object to move in horizontal direction.

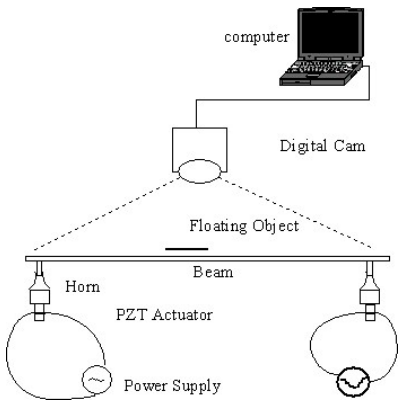

Figure 4. Scheme of Transportation System

When the beam starts to vibrate, the plate is rapidly levitated and gradually accelerated along the wave propagation direction by the viscous force [3]. The exact governing equation that describes the air velocity gradient and the effect on the transport speed of object has not been conducted out yet.

Experiment setup

The system consists one beam(400*50.8*3.175mm) and two Langevin type Transducer (BLT) manufactured by NTK (Model No. DA4427), which are attached to the beam at a length of $\lambda / 4$ from the end of the beam. When there is phase angle of 90 differences, the traveling wave is produced and the transportation direction can be changed by changing the phase difference between the two transducers. Since there is no support force across the width of the vibrating beam, the levitated levitation object is not stable and slides off easily during transportation. It is necessary to make appropriate vibration distributions across the plate in order to transport a levitated object stably. One traditional but effective method to make both ends thinner can obtain the desirable vibration distribution to prevent the plate falling off the beam. The system is excited at frequency of 25.6 KHz, which makes the most desirable traveling wave on the beam., When a flat plate (r=36.1mm mass=4g) is put on the vibrating beam, the plate is suddenly levitated and then gradually accelerated to a certain speed due to the near boundary streaming produced by traveling wave.

Due to the oscillation along the width direction, it is difficult to get the position using Laser displace meter. The author uses a simple but effective method –Web Cam to capture the motion and then utilizes Matlab to derive the position vs. time data.

The data process using Matlab

Using Matlab, the video captured by the web cam is analyzed.
The flow chart of derivation is shown in Figure 5. The video firstly is divided into frames and on each frame the plate is marked with darker dot in the center therefore the position can be obtained by calculating the intensity.

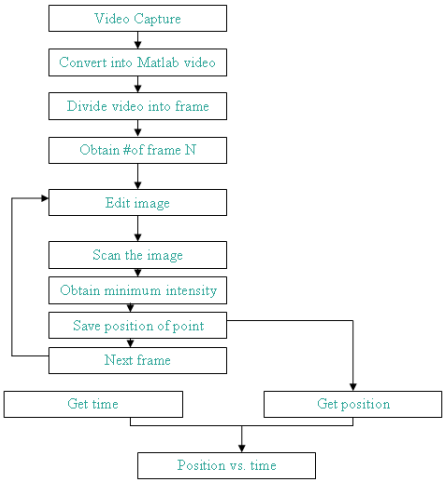

Figure 5. Derivation Flow Chart

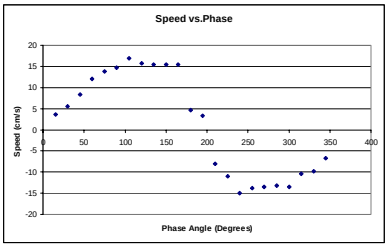

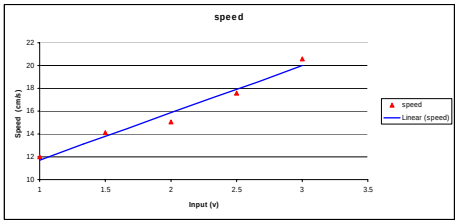

Figure 6. Steady-state velocity vs. Phase angle **Figure 7.** Steady-state velocity vs. Input voltage

Figure 6 shows the steady-state transportation velocity as a function of phase angle, it can be seen that when the phase angle between the two transducers reaches 90 degrees, the maximum steady speed of 0.18 m/s is achieved. When the phase angle changes to 270 degrees, the transportation direction will reverse and reach a maximum speed of -0.18m/s.

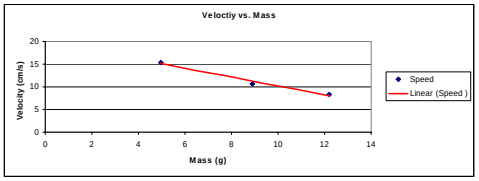

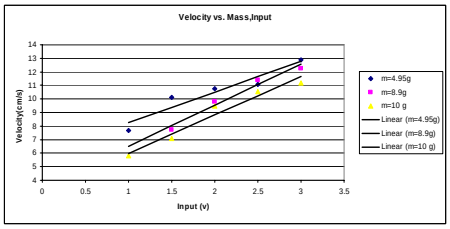

Figure 8. Steady-state velocity vs. Mass /Area **Figure 9.** Steady-state velocity vs. Input voltage

Figure 7~9 are the relationships between steady-state speed, input voltage and Mass Area ratio. It can be seen that in Figure 7 the steady-state speed increases when increasing the input voltage; in Figure 8 the steady-state speed decreases when the mass area ratio increases. This limits the application scope of such transportation systems with a flexural traveling wave; and Figure 9 is the steady-state velocity with respect of input voltage and mass area ratio.

Real time data derivation

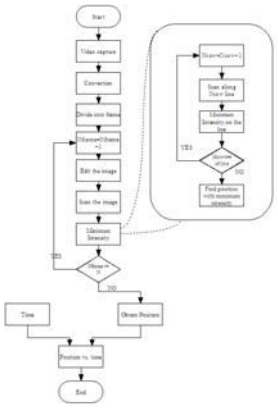

Figure 10. Flow chart for deriving the position vs. time

Another mechanism is programmed to get real time data. To facilitate use of the technique, the plate is marked with a dark dot at the center of the plate. The flow chart for the deriving data is shown in Figure 10. The video is captured and then imported into Matlab workspace. The video file is divided into frames, the RGB video is directly cropped to desired region, and converted into binary as shown in Figure11 (a)~(c), then passes through the embedded code. The position is derived with respect of time. Therefore the position can be obtained by calculating the intensity and the speed can then be obtained by differentiating derived displacement with respect to time.

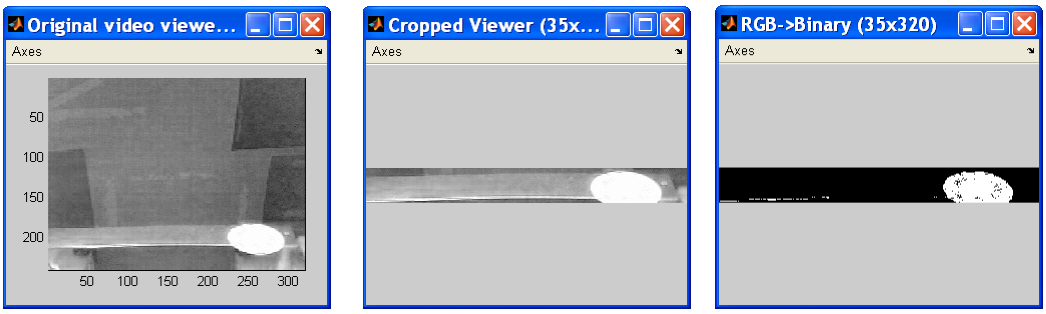

(a) Original video frame (b) Cropped video frame (c) Converted video frame

Figure 11. the edited video frame

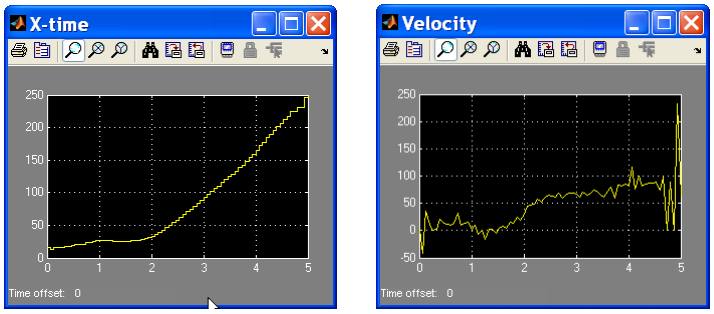

(a) X-position vs. time (b) Velocity vs. time

Figure 12. the derived position data

Figure12 is the real time derived position data from which it can be seen that the motion of plate is firstly gradually accelerated and then moves at constant speed, the velocity of the plate is about 18 cm/s.

The Floating Object Tracking Using Matlab

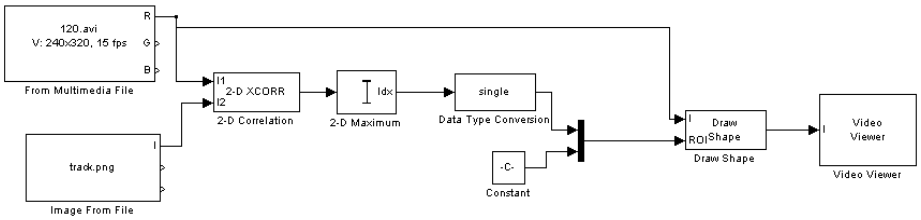

Figure 13. Simulink -Tracking Object

The simulink components are shown in Figure13. In this model the ***2-D Correlation*** block is to determine the portion of each video frame that best matches the image for tracking; the ***2-D Maximum*** block is to find the index of the maximum value in each input image.
The tracking results are shown below in Figure14:

Figure 14. Tracking results

9.3 CONCLUSIONS

It is concluded that NFAL can be achieved with flexural wave resource. The levitation distance is proportional to the vibration amplitude. The traveling wave can be produced by setting the phase angle of two transducers into 90 degree, and direction change can be achieved by reversing the phase angle into -90 degree. The transportation system is feasible and the stop-go control can be achieved by close loop control. It is helpful to incorporate beam and horn into one during the experiment setup. The non-contact transportation system can be devised based on NFAL and viscous force. The future work would be (1) Analytical approach; (2)Ansys analysis of system and simulation on air radiation;(3)Control of object transportation and (4) make the plate turn direction.

REFERENCES

1. Hideyui Nomura, Tomoo Kamakura and Kazuhisha Matsuda, ”Theoretical and experimental examination of near-field acoustic levitation,” J.Acoust.Soc.Am. 111(4),1578-1583,(2002).

2. Sadayuki Ueha, Yoshiki Hashimoto and Yoshikazu Koike,”Non-contact transportation using near-field acoustic levitation ,” Ultrasonics 38 ,26-32,(2000).

3. Yoshikau Koike,Sadayuki Ueha,Atsushi Okonogi, Takafumi Amano and Kentaro Nakamura,”Suspension Mechanism in Near field acoustic levitation phenomenon,” IEEE ULTRASONICS SYMPOSIUM,671-674,(2000)

4. Yoshiki Hashimoto, Yoshikazu Koike and Sadayuki Ueha, “Near-field acoustic levitation of planar specimens using flexural vibration,” J.Acoust.Soc.Am.100(4),2057-2061,(1996).

10 DESIGN TOOLS FOR FREEFORM OPTICS

Kenneth P. Garrard
Precision Engineering Center Staff
Thomas Dow
Professor
Department of Mechanical and Aerospace Engineering

10.1 INTRODUCTION

Freeform optical surfaces are defined as any non-rotationally symmetric surface or a symmetric surface that is rotated about an axis that is not its axis of symmetry. These surfaces offer added degrees of freedom that can lead to lower wavefront error and smaller system size as compared to rotationally symmetric surfaces [1,2]. Unfortunately, freeform optics are viewed by many designers as more difficult and expensive to manufacture than rotationally symmetric optical surfaces. For some freeform surfaces this is true, but a designer has little or no feedback to quantify the degree of difficulty for manufacturing a surface. This paper describes a joint effort by Optical Research Associates (ORA) and the Precision Engineering Center (PEC) at North Carolina State University to integrate metrics related to the cost and difficulty of manufacturing a surface into the merit function that is used during the design of an optical system using Code V®. By incorporating such information into the merit function, it is possible to balance optical performance and manufacturability early in the design process.

10.2 TECHNICAL OBJECTIVES

There were three technical objectives: first, develop a design environment that could support an optical designer with tools to assess the difficulty to manufacture (i.e. cost to manufacture) a freeform optical surface; second, demonstrate the usefulness of these new design tools by utilizing them during the redesign of an optical system; and finally, demonstrate the ability to evaluate the effect of manufacturing errors inherent in the fabrication of freeform surfaces.

10.3 RESULTS

10.3.1 DEVELOPMENT OF ENHANCED DESIGN ENVIRONMENT

This project developed an integrated design and optimization environment that brought together, for the first time, the existing optical performance predictions with automated feedback of

manufacturing costs of fast tool servo (FTS) machined freeform surfaces. Schematically, the project created the environment shown in Figure 1. The environment developed is quite powerful, general and extensible. However, the initial scope of this work was limited to surfaces that were off-axis sections of conic surfaces.

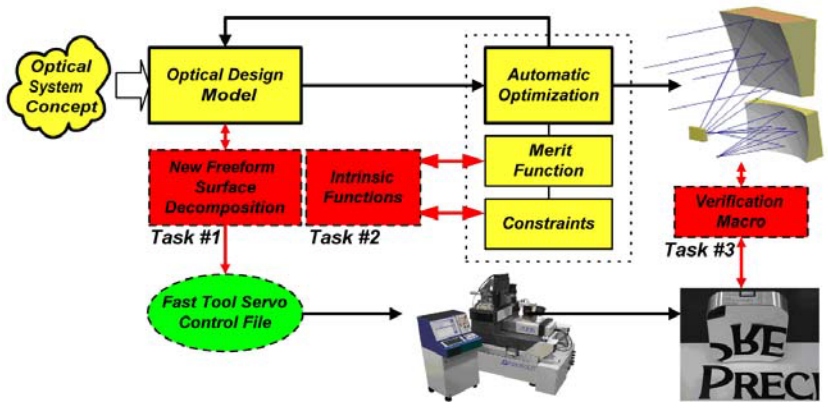

Figure 1. Integration of freeform surface decomposition with automatic optimization.

These sections are not rotationally symmetric about their center, and therefore have that characteristic of freeform surfaces that is most directly related to their difficulty to manufacture. In addition, the algorithm for decomposing such surfaces into rotationally symmeytric (RS) and non-rotationally symmetric (NRS) components had been previously worked out at the PEC for use as a real-time trajectory generator in a machine tool controller [3,4]. An implementation of this algorithm in C code was developed at PEC and provided to ORA.

The decomposition can provide useful information to a designer after surface shapes have been determined. However, maximum benefit is realized by giving the designer feedback during the actual optimization process. This can be done by using the NRS decomposition to generate appropriate metrics and by incorporating these metrics into the merit function that is used during the optimization process. The proper choice of a metric based on the surface decomposition would require a careful consideration of how a particular manufacturing process is able to generate a surface shape. While this is the ultimate goal of this research, a single metric was chosen that is a reasonable choice for a wide variety of manufacturing technologies. Specifically, the magnitude of the NRS component of the surface sag as a predictor of manufacturing cost.

Determination of the maximum NRS component of the sag is one of the output quantities computed by the decomposition C code. While it was possible to incorporate this code, with slight modifications, directly into CODE V to compute NRS sag during the optimization process, such an approach would lack the flexibility needed to allow generalization of this approach in the future. Specifically, it is anticipated that multiple manufacturing processes will need to be characterized. Each of these processes will have a unique fabrication cost function, and the objective was to design the code in such a way that it would anticipate such variations and allow them to be readily incorporated into CODE V in the future.

The goal was to structure the interface between the manufacturing cost metric computation and the optimization engine in a way that allowed maximum flexibility in the future, and also was as efficient as possible. Lens optimization is a very computationally intensive operation. All components of the merit function and all constrained quantities must be evaluated many times during a single optimization cycle. For this reason, it is desirable to perform these computations using code that has been optimized for speed. To achieve this goal, the interface was structured to rely on a dynamically linked library (DLL) implementation of the manufacturing cost metric. This allows the cost metric computation to be written in a standard language and compiled using an optimizing compiler. This approach required modifications to the CODE V MACRO-Plus language to allow external DLL routines to be accessed via a procedure call mechanism. It was also necessary to create an interface that would allow external DLL's to access information about the lens. This provides a mechanism for the DLL routine to query the lens to determine its surface shape.

The basic structure of the computations and interactions between the various computational components is illustrated in Figure 2. A user defined function (UDF), which will return a manufacturing cost metric, is written in CODE V's MACRO-Plus language. This UDF will call the DLL that actually performs the computation of the cost metric. In addition to surface shape information that the DLL is able to obtain directly from the lens database, it is also necessary for the UDF to compute information about the beam footprint of the surface. This information is determined by tracing the bundle of rays from each field point and by determining the footprints

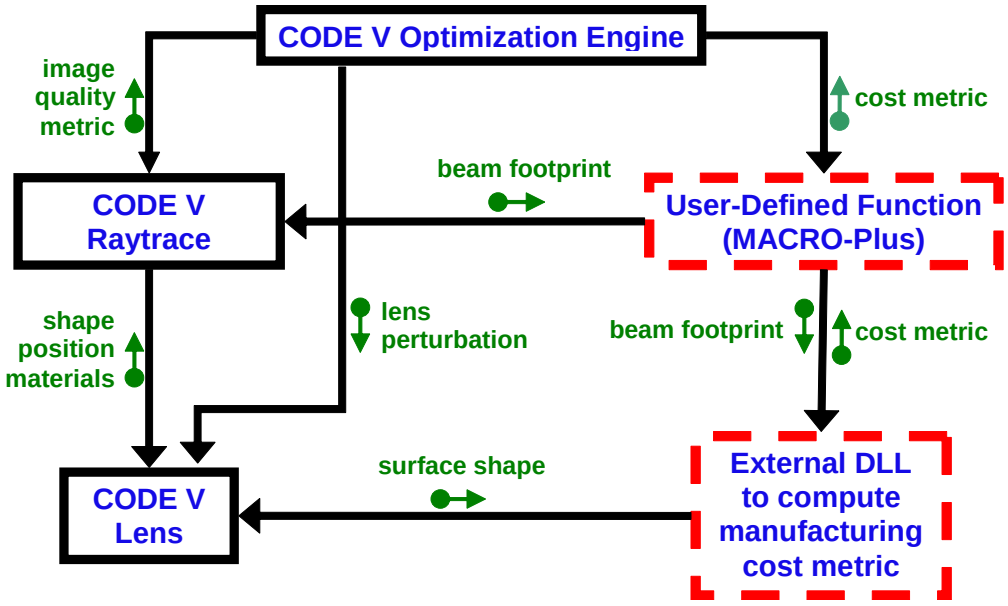

Figure 2. Interaction of components to compute a "manufacturing-aware" merit function.

of the beams (one beam from each field point) on the surface. The size of the "clear aperture" is required by the DLL when it performs decomposition.

10.3.2 DEMONSTRATION OF THE USEFULNESS OF THE "MANUFACTURING-AWARE" DESIGN ENVIRONMENT

To prove the benefits of this enhanced design environment, two existing optical systems were redesigned and optimized with respect to NRS sag. In each case, the original system contained aspheric components. The first step was to modify each of the systems to use conic surfaces. The first system was a three mirror, off-axis, unobscured system with conic surfaces for the first two mirrors and an asphere for the third surface. The asphere was replaced with a conic that did not significantly degrade performance. The basic layout of this system is shown in Figure 3. The second demonstration system was a four mirror system. Its optimization is described in [5].

Figure 3. Three mirror demonstration system.

The three mirror system covered a field of view of ±2 degrees. After the initial modification to include only conic surfaces, it had an average root-mean-squared wavefront error (RWE) of 0.091 waves (at a wavelength of 1 μm). Next the maximum NRS sag for each of the three mirrors was examined. The first mirror had a peak-to-valley (PV) NRS sag of 0.047 mm, the second mirror had a negligible PV NRS sag and the third mirror had a PV NRS sag of 0.056 mm. The maximum NRS sag was reduced in successive optimization runs using a UDF and the decomposition DLL function to constrain the maximum NRS sag to be less than or equal to a specified amount. For each NRS surface sag, the RWE was computed.

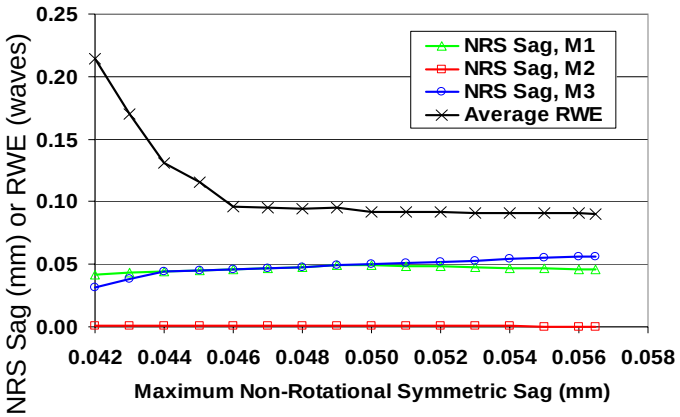

Figure 4. Behavior of RMS wavefront error (RWE) as a function of NRS sag for the three mirror system.

A plot of the results for the three mirror system is shown in Figure 4. In this case it is possible to

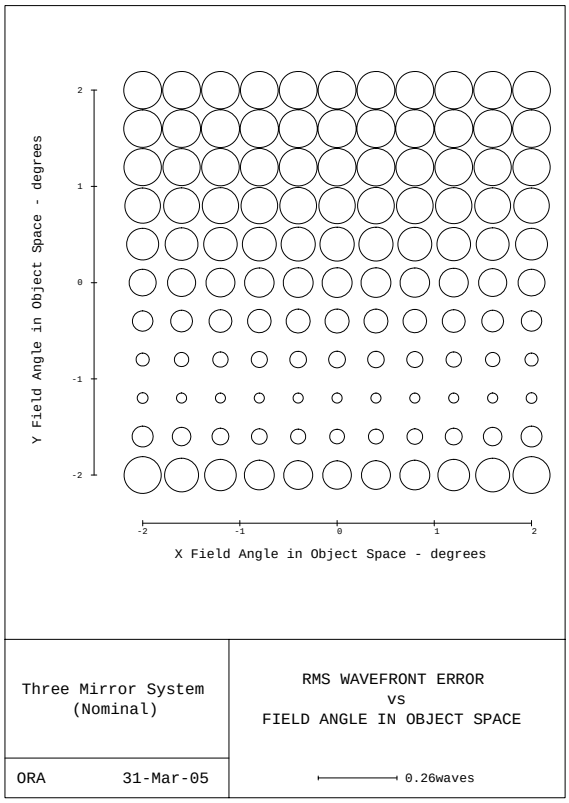

Figure 5. A display of the magnitude of the RMS wavefront error over the field of view for the redesigned three mirror system. For this system, the maximum NRS sag is 0.046 mm and the average RWE is 0.096 waves.

substantially reduce the PV NRS sag of mirror three (M3) without increasing the RWE. However, as the NRS sag of M3 starts to get smaller than that of mirror one (M1), the maximum NRS sag is now determined by the NRS sag of M1. Reducing the NRS sag of this mirror has a much more dramatic impact on the RWE. For this optimized system, Figure 5 shows the distribution of RWE over the ±2 degree field of view. With a maximum NRS sag of 0.046 mm (on mirror one), the RWE can be kept below 0.1 waves. Further reductions in NRS sag lead to sharp increases in RWE.

This study of optical performance versus manufacturability was simple to accomplish with the software tools developed. A study such as this would not have been possible without this new design tool. The benefit to a designer is quite clear: At an early stage of a design, it is possible to consider manufacturability aspects of a system. Tradeoffs between performance and cost that allow an appropriate balance between these two conflicting goals can be quickly evaluated. In the absence of this feedback, it is easy for a designer to chase higher performance designs without realizing the cost that will be incurred during the fabrication of the system.

10.3.3 SIMULATION OF FABRICATION ERRORS

For an optical design environment to be truly “manufacturing-aware,” it must be able to simulate the expected manufacturing errors for manufacturing processes. The goal was to gather data about such process errors and to perform a realistic simulation of some of the fabrication errors for one of the demonstration systems (the three mirror system.) In particular, the surface figure errors that would be expected due to the dynamics of a Variform FTS system were considered. Once these errors were simulated, their effect on the optical performance was evaluated by constructing an interferometric error map which was then inserted into CODE V to determine the

impact of the machining process on the performance of the optical design. The error map mimics the result of measuring a surface with an interferometer and an appropriate null reference (e.g., a Zygo GPI and a computer generated hologram).

The NRS shape of mirror one from the three mirror system is shown in Figure 6 and requires a 46 µm excursion of the FTS to machine in an on-axis orientation. To produce a simulated error map the NRS shaped was first transformed into a time-based signal for typical machining conditions (e.g., 1200 rpm spindle rotation), convolved with the dynamics of the Variform FTS and interpolated onto a 256 x 256 point Cartesian grid. This error surface is shown in Figure 7. Note that the total range of the error is 5.8 µm over the entire aperture, which has a sag of 2.5 mm. The error is predominately due to phase lag in the actuator response at the 20 Hz rotational velocity of the machining spindle. The magnitude of this error can be reduced by either advancing the phase of the actuator command signal or by slowing down the spindle. Errors were simulated with no correction (i.e. no phase advance) applied (Figure 7), and also for the case where a fixed time advance was applied to the drive signal to reduce the effect of actuator dynamics. The result shown

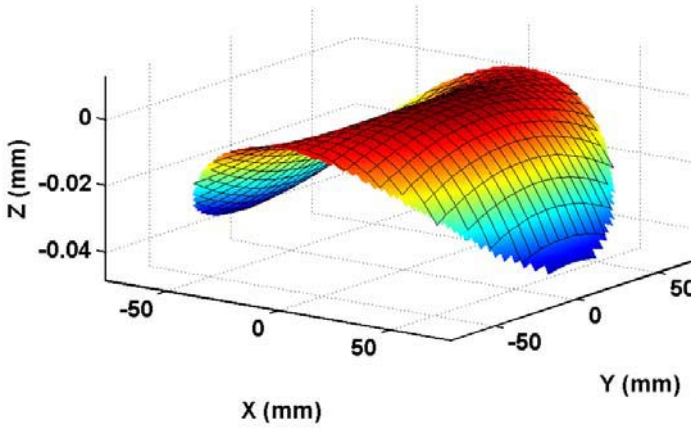

Figure 6. The magnitude of the NRS component of the surface sag for mirror one of the three mirror system.

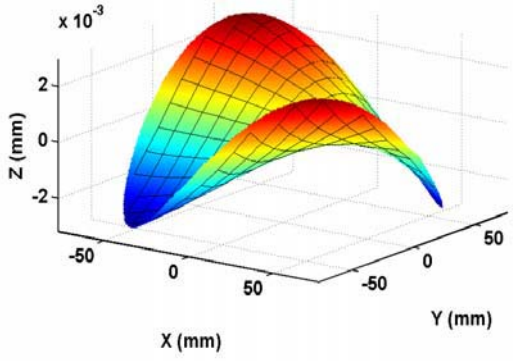

Figure 7. The simulated surface figure errors for mirror one of the three mirror system. This simulation was performed without a correction to counteract the actuator dynamics.

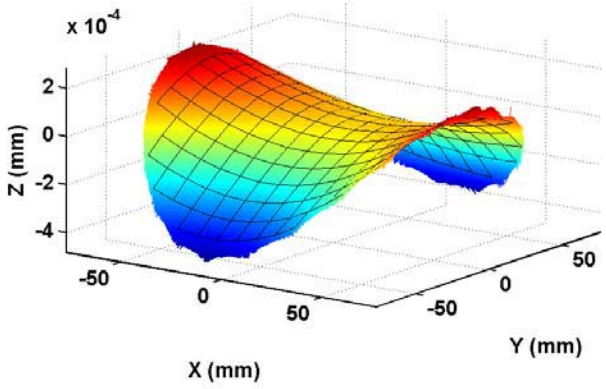

Figure 8. The simulated figure errors for mirror one of the three mirror system. This simulation was performed with a correction for the actuator dynamics.

in Figure 8 is a plot of the simulated figure errors with the fixed time advance correction applied to the drive signal.

The important difference to note between the figure errors shown in Figures 7 and 8 is the difference in the magnitude of the errors. A simple correction for the actuator phase lag has reduced the errors from 5.8 μm (Figure 7) to 650 nm (Figure 8). A second subtle difference between Figures 8 and 9 is that the angular orientation of the figure error has changed.

When the as-built system is modeled using the fabrication process with a drive signal without correction for actuator dynamics, the RWE figure increases to 0.367 waves, nearly a 4x increase in the RWE. The RMS wavefront error over the full-field is displayed in Figure 9. When the figure errors produced with the fabrication process that accounts for actuator dynamics are added to the system model, the optical performance of the system actually improves as shown in Figure 10.

The average RWE for the system, which was 0.096 waves for the nominal design (see Figure 5),

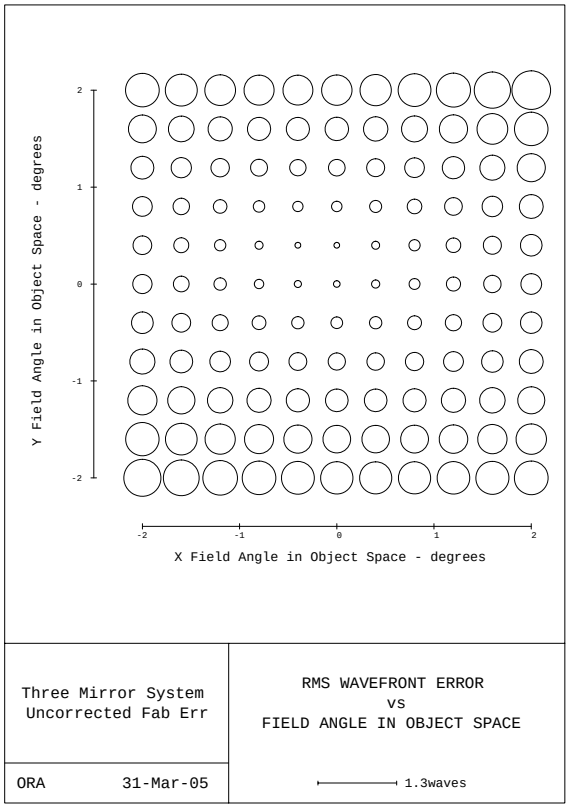

Figure 9. The RMS wavefront error of the simulated, as-built three mirror system without actuator dynamic correction.

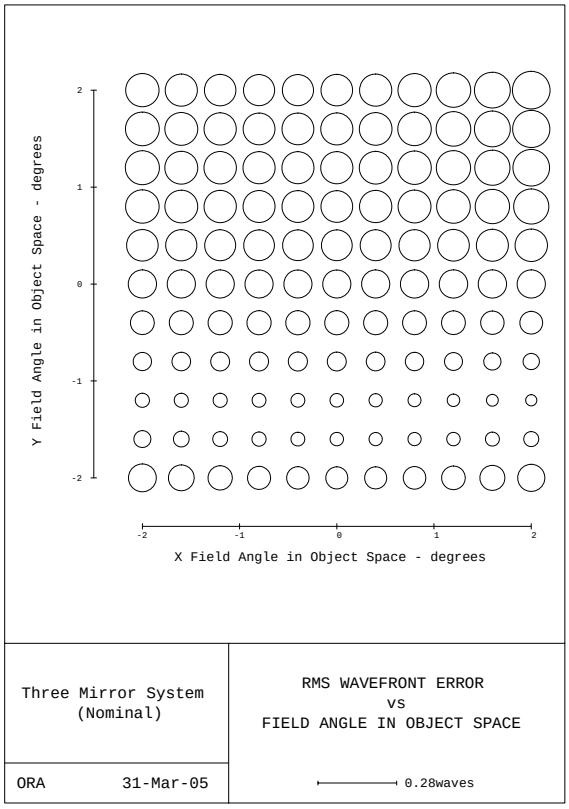

Figure 10. The RMS wavefront error for the simulated as-built three mirror system with actuator dynamic corrections.

was reduced to 0.093 waves. This effect is apparently due to the fact that the surface errors create a surface form that was not allowed in the original optimization process. That is, the as-built surfaces are not actually off-axis sections of conic surfaces. The fabrication errors have created different surfaces, which actually produce a slightly better image quality. While such results are unusual, the important fact to note is that the fabrication errors have been modeled and a designer can have confidence in the ability of the as-built system to meet the requirements.

10.4 CONCLUSIONS

The ability of an optical designer to obtain early feedback about the manufacturability and cost of a freeform surface will ultimately lead designers to employ these surfaces in those designs where the benefits are worth the added cost. In the past, it has been the case that a designer is completely unsure of what that added cost is, and thus there is no easy way for a compromise between cost and performance to be made for systems utilizing freeform shapes.

This project has taken the following significant steps toward the ultimate goal of a "manufacturing-aware" design process by:

1. Adding functionality to the CODE V optical design program that allows it to compute metrics that are related to cost and difficulty of fabricating NRS surfaces.
2. Incorporating the cost metrics for NRS surfaces into the merit function or into constraints that are used during the optimization. This allows the optimization process to automatically trade off performance versus cost.
3. Demonstrating the benefit of items (1) and (2) by performing a design using the new capability.
4. Demonstrating the ability to characterize a manufacturing process in a way that allows the prediction of surface figure errors for a specific profile.
5. Predicting the as-built performance of a system by incorporating the predicted surface figure errors into the model of the nominal design.

ACKNOWLEDGEMENT

This work was supported by the United States Army Space and Missile Defense Command under STTR contract W9113M-04-P-0149.

REFERENCES

1. Rodgers, M. and K. Thompson. Benefits of freeform mirror surfaces in optical design. Proceedings of the ASPE 2004 Winter Topical Meeting on Freeform Optics, 31, 73-78 (2004).

2. R.G. Ohl, A. Sohn, T.A. Dow and K.P. Garrard. Highlights of the ASPE 2004 winter topical meeting on freeform optics: design, fabrication, metrology, assembly. Proceedings of the SPIE 5494, (2004).

3. W.D. Allen, R.J. Fornaro, K.P. Garrard and L.W. Taylor. A high performance embedded machine tool controller. Microprocessors and Microprogramming, 40, 179-191, (1994).

4. United States patent 5,467,675. Apparatus and method for forming a workpiece surface into a non-rotationally symmetric shape. Thomas A. Dow, Kenneth P. Garrard, George M. Moorefield, II and Lauren W. Taylor (1995).

5. Garrard, K., T. Bruegge, J. Hoffman, T. Dow and A. Sohn. Design tools for freeform optics. SPIE 5874 (2005).